Astronomy & Astrophysics manuscript no. rho_ophiuchi_aa
May 25, 2016
©ESO 2016

The first stars of the *Rho Ophiuchi Dark Cloud.*

XMM-Newton view of Rho Oph and its neighbors.

I. Pillitteri[1,2], S. J. Wolk[2], H. H. Chen[2], and A. Goodman[2]

[1] INAF-Osservatorio Astronomico di Palermo, Piazza del Parlamento 1, Palermo, 90147 – Italy e-mail: pilli@astropa.inaf.it
[2] SAO-Harvard Center for Astrophysics, 60 Garden St, Cambridge, 02138, MA – US

Received; accepted

arXiv:1605.07365v1 [astro-ph.SR] 24 May 2016

ABSTRACT

Star formation in molecular clouds can be triggered by the dynamical action of winds from massive stars. Furthermore, X-ray and UV fluxes from massive stars can influence the life time of surrounding circumstellar disks. We present the results of a 53 ks *XMM-Newton* observation centered on the ρ Ophiuchi A+B binary system. ρ Ophiuchi lies in the center of a ring of dust, likely formed by the action of its winds. This region is different from the dense core of the cloud (L1688 Core F) where star formation is at work. X-rays are detected from ρ Ophiuchi as well as a group of surrounding X-ray sources. We detected 89 X-ray sources, 47 of them have at least one counterpart in 2MASS+*All-WISE* catalogs. Based on IR and X-ray properties, we can distinguish between young stellar objects (YSOs) belonging to the cloud and background objects. Among the cloud members, we detect 3 debris disk objects and 22 disk-less – Class III young stars. We show that these stars have ages in 5 – 10 Myr, and are significantly older than the YSOs in L1688. We speculate that they are the result of an early burst of star formation in the cloud. An X-ray energy of $\geq 5 \times 10^{44}$ ergs has been injected into the surrounding medium during the past 5 Myr, we discuss the effects of such energy budget in relation to the cloud properties and dynamics.

Key words. Stars: activity – Stars: formation – X-rays: stars – Stars: individual: Rho Ophiuchi – open clusters and associations: general

1. Introduction

The action of an external agent onto an initial gas cloud is invoqued to create gas instabilities and lead to the formation of the protostellar cores (Elmegreen 1998). While supernova explosions are one possible agent, another is the action of the stellar winds from massive stars and the expansion of ionized HII bubbles that can transfer momentum, kinetic energy and heat to a nearby gas cloud.

Understanding the star formation history of a cloud requires an indicator of age and evolutionary status. The ratio of stars without disks to stars still bearing a disk can be used to assess the degree of evolution of the process of star formation in a gas cloud (Strom 1995; Haisch et al. 2001; Gutermuth et al. 2009), but assessing a complete census of both classes of objects is difficult. For regions distant more than 1 kpc, proper motion studies have insufficient sensitivity, photometric selection is strongly contaminated by field stars, and spectroscopic selection requires an enormous effort to study hundreds or thousands of stars – even when using new multi-fiber facilities. Infrared (IR) studies are helpful (when crowding is not extreme), but they are sensitive only to stars with circumstellar material, bright in IR, but insensitive to objects without disks, i.e., Class III Pre Main Sequence (PMS) stars (Lada & Adams 1992). However, PMS stars are up to 10^3 brighter than the Sun in X-rays, and this fact can be used to effectively detect young disk-less members of star forming regions and in young associations.

The complex of Rho Ophiuchi Dark Cloud is a patchy, multi-core cloud that spans a few degrees in the sky near the eponymous system ρ Ophiuchi. A range of distances to the cloud are reported in literature (Wilking et al. 2008), spanning the range 120 pc to 145 pc; here we will use the distance of 120 pc, obtained from VLBI measurements by Loinard et al. (2008) and valid for the northern part of the cloud where ρ Ophiuchi is located. The uncertainty on the distance can produce a systematic error of the X-ray luminosities of $\sim$ 0.16 dex. The main core of the cloud, L1688, contains high density gas and dust and a stellar population of about 300 Young Stellar Objects (YSOs, Gagné et al. 2004; Wilking et al. 2005). The dense core F of the cloud has been extensively studied in infrared and X-rays. In X-rays, several *Chandra* observations have targeted L1688 for a total duration of about 400 ks (Imanishi et al. 2001; Gagné et al. 2004).*XMM-Newton* has also observed L1688 with a 35 ks exposure (Ozawa et al. 2005), and with a large program named DROXO (PI: S. Sciortino, exposure $\sim$ 500 ks) aimed at obtaining a deep observation to characterize the X-rays properties of the YSOs embedded in the L1688 core (Giardino et al. 2007; Flaccomio et al. 2009; Pillitteri et al. 2010). X-ray surveys have demonstrated the frequent variability of YSOs in L1688 (see Montmerle et al. 1983), and the first cases of detected neutral Fe line at 6.4 keV in stellar X-ray spectra, due to the interaction of high energy photons from the central object and cold material in the circumstellar disk.

In the present work, we investigate a region north to the Cores F and A of the cloud, centered on ρ Ophiuchi A+B (Fig. 1), where a partially open ring of dust is visible in mid and far IR images from *Spitzer*-MIPS and IRAS (Schnee et al. 2005). The ring or shell was likely formed by the stellar winds of B stars at its center. Other similar structures are reported in literature. With GLIMPSE, Churchwell et al. (2006) detected 322

Table 1. Log of the *XMM-Newton* observation.

R.A. (J2000)	Dec. (J2000)	Filter	Exp. Time ks	ObsID
$16^h25^m30.0^s$	$-23^d28^m00.0^s$	Thick	53	0720690101

partial and closed rings. They argue that the bubbles are primarily formed by hot young stars in massive star formation regions and about 13% enclose known star clusters. Only three of the bubbles are identified with known SNRs, and no bubbles coincide with known planetary nebulae or W-R stars; this suggests that B stars can effectively produce such bubbles. In a study of similar structures in the Perseus cloud, Arce et al. (2011) suggested that bubbles like the one in ρ Ophiuchi are formed by the interaction of spherical or very wide angle winds powered by the young stars inside. Two of the twelve shells observed in Perseus are powered by high-mass stars close to the cloud, while the others appear to be powered by low- or intermediate-mass stars in the cloud. Arce et al. (2011) argue that winds from stars with a mass loss rate of about 10^{-8} $M_\odot$ yr^{-1} to 10^{-6} $M_\odot$ yr^{-1} are required to produce the observed shells.

A portion of the warm dust ring around ρ Ophiuchi has been partially observed in X-rays with ROSAT (Snowden 1994; Casanova et al. 1995; Martin et al. 1998). Due to the low PSPC sensitivity and partial spatial coverage, only a handful of X-ray sources are reported in the region. Martin et al. (1998) noticed that the ratio of Class III to Class II objects (or WTTSs to CTTSs in their terminology) is 10:1 in this region. They suggested that this high ratio could be attributed to the action of the stellar winds from ρ Ophiuchi on the nearby disks and not ascribed entirely to an evolutionary effect.

With the present *XMM-Newton* observation we obtain a more complete census of disk-less stars around ρ Ophiuchi, and we aim to understand the impact of the clearing action that ρ Ophiuchi has made in the surrounding interstellar medium. We will relate the star formation history in this part of the cloud to that of L1688, and, with the use of X-rays and IR data, we aim to quantify how many YSOs are formed in this region and their evolutionary stage. The paper is structured as follows: in Sect. 2 we describe the observations and the data analysis, in Sect. 3 we report the results, in Sect. 4 and 5 we discuss our findings and present our conclusions.

2. Observations and data analysis

The system of ρ Ophiuchi A+B ($\alpha = 16^h25^m35.12^s$; $\delta = -23^d26^m49.8^s$) is composed by a B2IV and a B2V type stars, respectively. The system has been observed with *XMM-Newton* on August 29th 2013; Table 1 reports the details of the observation. Due to the UV brightness of ρ Ophiuchi, we used the *Thick* filter to prevent optical photons from triggering spurious events in the EPIC camera, which was set as primary instrument, and the OM instruments was not used.

We reduced the ODFs with SAS ver. 13, then we filtered the event tables in the 0.3−8.0 keV band, selected only events which triggered at most four adjacent pixels (PATTERN< 12) and with FLAG = 0. Toward the end of the exposure when the satellite was approaching the orbital perigee, the background level increased. The effect is prominent in PN data, while it is negligible in MOS detectors. We filtered out this high background interval from the PN exposure, following the recipe from SAS guide and removing the last 5 ks. Fig. 1 (inset image) shows a RGB composite image of EPIC data (MOS 1, 2 and PN), with colors of the sources qualitatively indicating the hardness of their spectra. We chose the following ranges for the RGB channels: $R = 0.3 - 1.0$ keV; $G = 1.0 - 3.0$ keV; $B = 3.0 - 8.0$ keV. The choice of these energy bands is effective in selecting sources characterized by thermal/coronal emission and sources with heavily absorbed and harder spectra. Sources with soft spectra show yellow/red colors, while sources with harder spectra show blue colors. We used this visual attribute to choose the type of model for fitting the spectra of sources with enough count statistics.

For the source detection process, we applied a wavelength convolution algorithm derived from the analog code developed for ROSAT (Damiani et al. 1997b,a) and Chandra. The *XMM-Newton* version allows an analysis on the sum of MOS and PN data maximizing the efficiency of the detection toward the faint sources. We used a threshold of significance equal to 4.6 σ, that statistically retain, at most, one spurious source due to background fluctuations.

Spectra and light curves of the sources have been obtained by selecting the events from circular regions around the positions of the sources, and choosing their radii in order to avoid contamination from nearby sources. Typical extraction radii were 15″ to 20″. For background regions, we followed the prescription of SAS guide, in particular for PN used regions that are approximately at the same distance of the source from the read out node, because of the changing response along the chip.

The spectra were analyzed with XSPEC ver. 12.8 (Arnaud et al. 1999) with two types of models: thermal APEC models (up to three components) plus global absorption for coronal sources, and power law spectra plus global absorption for low count statistics spectra and for sources with a hard spectrum. The aim was to infer N_H absorption, characteristic plasma temperatures and emission measures of the thermal components for the coronal sources, and power law indices and normalization factors for the sources with hard spectra or with poor count statistics. In Table D.1 we report the results of the best fit to spectra and the parameters: N_H absorption, temperatures, normalization factors, power law indices, fluxes in 0.3-8.0 keV band, and χ^2 statistics.

3. Results

We have detected 89 sources at a significance threshold > 4.6σ of the local background. In Table B.1 we list the coordinates, count rates, off-axis distance and statistical significance in units of standard deviation (σ) of local background fluctuation. To evaluate the nature of the X-ray sources we use the results of Getman et al. (2011), that estimated the number of contaminants in the Chandra survey of Carina Nebula (Townsley et al. 2011). These numbers strongly depends on several parameters including the model for galactic stars (foreground and background), galactic sources of different nature (e.g., compact objects), extragalactic sources, distance to the star forming region, extinction, and surveyed area. From scaling the numbers given by Getman et al. by the survey coverage, we estimate that about 10 foreground stars and a similar number of background stars should be detected in the *XMM-Newton* FOV, with many of these objects having WISE counterparts. In addition, about 30 extragalactic sources should be detected in X-rays, but probably they remain below the sensitivity of WISE. Out of the 89 X-ray sources, 42 of them are without either a WISE or 2MASS counterpart. In the following sections we will show that the stars related to the ρ Ophiuchi cloud and in the *XMM-Newton* field of view are characterized by an age of $\sim 5 - 10$ Myr and extinction of $A_V \sim 3$ mag. Disk-less stars at 120 − 145 pc, characterized by such age and extinction values, are easily detectable in X-rays

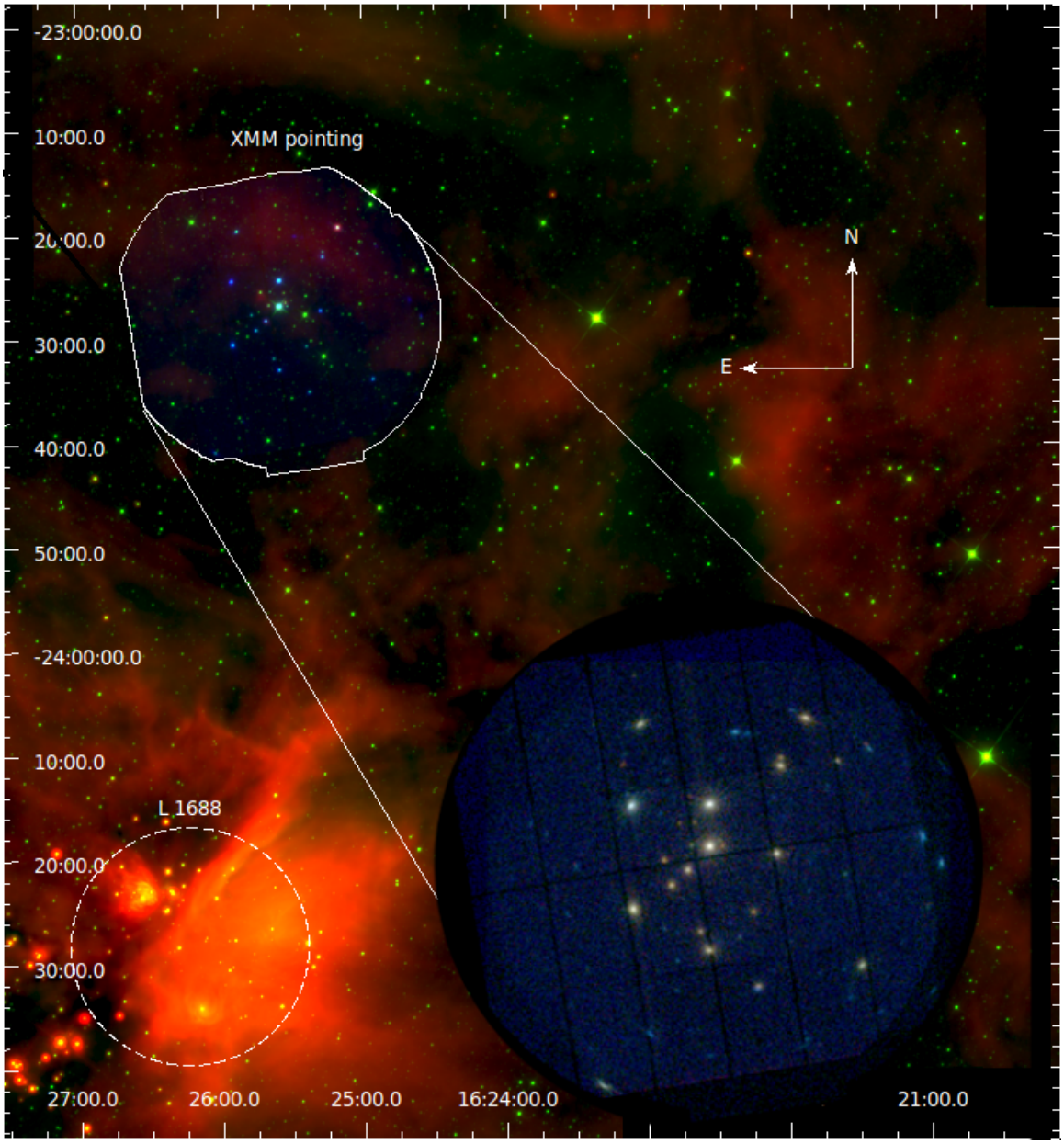

Fig. 1. Main panel: composite RGB image of WISE images and X-rays. Channel bands: blue = EPIC 0.3-8.0 keV; green = 3.4μm; red = 22 μm. We indicated the *XMM-Newton* pointing and the L1688 region which has been extensively studied. ρ Ophiuchi sits at the center of a ring of warm dust that has likely been cleared by its stellar winds. Inset image: composite RGB image of EPIC MOS and PN. Channel bands: red = 0.3-1.0 keV; green = 1.0-3.0 keV; blue = 3.0-8.0 keV. Different colors of the *XMM-Newton* sources indicate soft (yellow) or hard (blue) X-ray spectra.

and WISE/2MASS. The absence of near/mid- IR counterparts implies that, on average, these sources have distances not closer than 500 pc, and thus they are not related to the cloud. A visual inspection of the X-ray image shows that these are mostly faint sources, with detection significance comprised in the range $6.6 - 11.8\sigma$ of local background (10% – 90% quantiles range). Their cumulative spectrum is harder than the average spectrum of coronal sources belonging to the cloud. The median of energy of the 42 sources with no WISE/2MASS counterpart is $\sim$ 2 keV, with 90% quantile above 6 keV, while the sources likely related to the cloud have a median of $\sim$ 1 keV, and 90% quantile around 2 keV. The 42 sources are also spread uniformly across the *XMM-Newton* field. We conclude that these 42 sources cannot be related to the cloud, and are likely background objects.

The remaining 47 X-ray sources are associated with WISE objects, some of them mostly clustered towards the center of the XMM field. In section 3.1 we classify the WISE objects with X-ray detection based on their mid IR photometry. About 50% of these appear to be YSOs and members of the ρ Ophiuchi cloud.

We detected X-ray emission from ρ Ophiuchi A+B (source nr. 50, details in Pillitteri et al. 2014), ρ Ophiuchi C (source nr. 62, B5V star with a low mass companion, details in Sect. 3.5.2) and from Haro 1-4 (DoAr 16, spectral type K4, source nr. 84) which is the only Classical T-Tauri star (CTT) in the *XMM-Newton* field of view. ρ Ophiuchi D (HD 147888), which is a system with two B3/B4 stars, is undetected, this fact hints that X-ray emission among B type stars is either peculiar (like in ρ Ophiuchi A+B), or requires a low-mass companion (this could be the

case for ρ Ophiuchi C discussed in Sect. 3.5.2, see also Gagné et al. 2011 and references therein).

3.1. Infrared counterparts to X-ray sources

The Dark Cloud of Rho Ophiuchi has been observed with *Spitzer* as part of the *Cores to Disks* (*C2D*) program Evans et al. (2003), devoted to a deep IR scrutiny of the YSOs in the closest Star Forming Regions (Gutermuth et al. 2009, 2011; Kryukova et al. 2012). However, the region around ρ Ophiuchi and in the field of view of our *XMM-Newton* observation has not been observed with *Spitzer* IRAC.

In order to classify the objects with infrared excesses, we used IR photometry from *All WISE* catalog (Wright et al. 2010). We adopted the scheme of classification described by Koenig & Leisawitz (2014), which uses cuts in WISE colors and magnitudes to classify the YSOs in Class I, Class II and Transition Disks Objects (also named Debris Disks, hereafter DDs). The classification can distinguish YSOs from background AGNs or star-forming galaxies, which IR colors can be similar to YSOs but AGNs have fainter magnitudes than YSOs at the distance of Rho Oph. Figure 2 shows different color-magnitude and color-color diagrams obtained from *All WISE* photometry of objects in the *XMM-Newton* field. Later in Fig. A.1 we show similar plots for the objects in L1688 core. In Sect. 4 we discuss the difference of objects with disks and without disks in L1688 and around ρ Ophiuchi and the implications for the ages of YSOs and star formation history in the cloud.

At 9.5′ from ρ Ophiuchi, Haro 1-4 is classified as a Herbig Ae/Be star with strong Hα emission (Maheswar et al. 2003). The scheme of IR classification we adopted fails to assign it to the Class II / disk stars sample. The reason is that the photometry in 3.4μm band is not reliable as required by the scheme and thus Haro 1-4 is formally unclassified.

In Fig. 2 we denoted the X-ray sources with WISE counterparts with open squares. Among these objects, there are 22 X-ray sources relatively bright in WISE ([4.6]< 12). These objects tend to cluster around (0,0) in the [3.4] − [4.6] vs. [4.6] − [12] color-color diagram (marked with crosses in the WISE diagrams). We use X-ray detection as a criterion to classify these objects as young stars with X-ray bright coronae and normal photospheres. These stars are the disk-less members of the "Rho Ophiuchi cluster". Cuts in magnitudes and colors used to denote the loci of Class III stars are shown in Fig. 2, these cuts correspond to: [4.6] − [12] ≤ 0.8 mag, [3.4] − [12] ≤ 1.1 mag, and [3.4] − [4.6] ≤ 0.3 mag.

In the same color-color diagram, the DDs, Class II YSOs and Class I YSOs form a sequence distinct from the bulk of background star-forming galaxies and AGNs, which are also faint ([4.6] > 12) in the other WISE color-magnitudes diagrams. The value [4.6] ∼ 12 corresponds to a spectral type of M6 and $T_{\rm eff}$ ∼ 3000 K at the distance of ρ Ophiuchi (Siess et al. 2000). The value [4.6] < 12 allows us to distinguish between YSOs at the distance of ρ Ophiuchi (120 pc) and background objects. This is analogous to the cut in IRAC [4.5] magnitude we adopted in Pillitteri et al. (2013) to filter out faint background objects in Orion A at d∼ 415 pc with [4.5] > 14. This selection is valid only around ρ Ophiuchi, where extinction is much lower than, eg.g., in L1688 core. Moreover, the few Class II and Class I YSOs fainter than [4.6] = 12 are likely not members of the ρ Ophiuchi cloud. In particular, this is true for source nr. 81, which has IR counterpart classified as a faint Class I YSO. However, it has a hard X-ray spectrum which is best fit by a power law, its WISE [4.6] magnitude is 14.11 and thus it looks too faint to be a cluster member. For these reasons we excluded source nr. 81 from the list of cluster members.

Only 3 objects are questionable in the range 12 < [4.6] < 13 and none of them is classified as Class II or Class I. In Fig. 2, bottom right panel, objects with [3.4] − [4.6] > 0.4 have also [4.6] − [12] > 2.5. As shown in top right panel, all objects with [4.6] − [12] > 2.5 have [4.6] ≥ 14 but one, which has [4.6] − [12] ∼ 3 mag and [4.6] ∼ 12 mag. However, this object is not classified as a Class II YSO and still remains too red to be a Class III star or a DD objects as well.

In Fig. 3 we show the color-color and the color-magnitude diagrams from 2MASS photometry for objects around ρ Ophiuchi and, for comparison, for objects in L1688. The color-color diagram is useful to classify different IR classes of YSOs (Lada & Adams 1992) when using only J, H, and K_s bands. The isochrones at 5 and 10 Myr (Siess et al. 2000) are traced, as well the reddening vector corresponding to A_V = 3 mag. This value of visual extinction corresponds to an $E(B-V) \sim 1$ mag, which is derived from dust extinction probed by IRAS 100 μm images (Schlafly & Finkbeiner 2011). Objects near ρ Ophiuchi and with X-ray detection are lightly extincted. A few objects suffer $A_V \leq 2$ mag and all of them fall within the reddening strip of absorption/extinction solely expected to intervening material along the line of sight. These objects correspond to the Class III sample with no IR excesses. By comparison, Class II objects are redder in $H - K_s$ color due to the extra emission from their inner disks, and thus they fall on the red side of the reddening strip.

In summary, we obtained a classification of the WISE counterparts of the X-ray sources and identified 22 Class III stars and 3 DDs emitting X-rays, these are identified as young members of the "Rho Oph cluster". To these stars we add also ρ Ophiuchi itself, ρ Ophiuchi C, ρ Ophiuchi D (undetected in X-rays) and Haro 1-4, and these stars constitute the most massive members of the cluster. It is unlikely that we have missed any Class III stars faint in X-rays because the limit sensitivity of the exposure corresponds to $\log L_X \sim 27.7$ dex at the distance of 120 pc, while the typical luminosity of Class III stars is in the range $28.5 < \log L_X < 30$ dex. The paucity of Class I/II YSOs in the *XMM-Newton* field points to a real difference of age and evolutionary stage of YSOs in this region with respect to L1688. This will be discussed later more in details with the support of the result of fitting to isochrones of temperatures and bolometric luminosities.

3.2. SEDs, effective temperatures, bolometric luminosities, masses and ages

We used VOSA[1] web service (Bayo et al. 2008) to retrieve and fit the Spectral Energy Distributions (SEDs) of the counterparts to X-ray sources. We searched the available photometry of objects within a radius of 6″ from the X-ray positions. We restricted our analysis to the X-ray sources that are likely associated to the cloud, and thus the Class III stars, the DDs, ρ Ophiuchi A+B and ρ Ophiuchi C. We assumed a distance of 120 ± 10 pc and a visual extinction $A_V = 3 \pm 1$ mag. The SEDs were fit with several models: black-body, BT-COND (Allard et al. 2012), BT-DUSTY (Allard et al. 2012), BT-NEXTGEN-GNS93 (Allard et al. 2012), COND00 (Allard et al. 2001; Baraffe et al. 2003), DUSTY00 (Allard et al. 2001; Chabrier et al. 2000). The models depend on a set of parameters, including, e.g., $T_{\rm eff}$ for the black-body, and $\log g$, metallicity, alpha elements enhancement factor for the various versions of BT/NEXTGEN models. The number of points

[1] http://svo2.cab.inta-csic.es/theory/vosa4/index.php

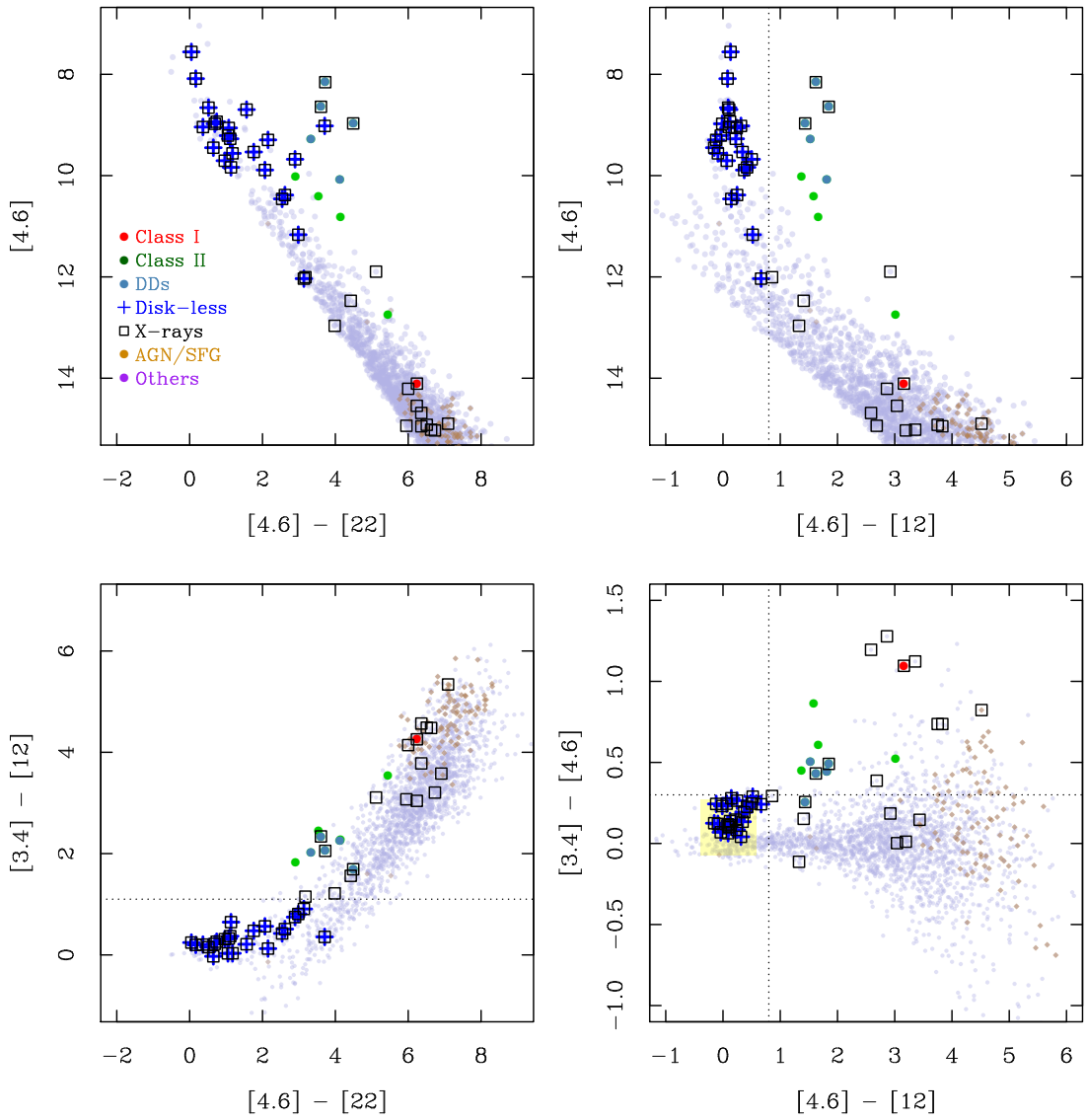

Fig. 2. WISE color-magnitude diagrams (top panels) and color-color diagrams (bottom panels) for WISE objects within the field of view of *XMM-Newton* ($\sim 16'$ from ρ Ophiuchi). Symbols are described in the legend in top left panel. In particular, we mark with squares the objects with X-ray emission, and with crosses the objects with colors typical of normal photospheres (thus not classified as Class I, II or DD objects) that have X-ray detection and [4.6] < 12 mag. Their number are 22 and are associated with Class III stars. Cuts in magnitudes and colors are marked with dotted lines, these correspond to: [4.6] – [12] = 0.8 mag, [3.4] – [12] = 1.1 mag, and [3.4] – [4.6] = 0.3 mag. Very few Class I and Class II YSOs compared to Class III stars are found in the FOV of *XMM-Newton* (cf. Fig. A.1 in Appendix).

in each SED, i.e., the amount of photometry available for each object and its quality, is crucial for a robust estimate of the best fit parameters of the SEDs. In particular, for a number of objects the photometry in U, B, and V bands is missing due to the moderate extinction in the region (of order of $A_V \sim 3.8$ mag). This has the effect of making the shape of the SED uncertain. Even in the simplest case of black-body model, the peak of the SED and the $T_{\rm eff}$ have errors associated with these color uncertainties. Also, the reliability of $L_{\rm bol}$ is a function of the assumed distance and of the extinction. Masses and ages depend on the fit to the isochrones (done through VOSA), and depend on the estimates of $T_{\rm eff}$, $L_{\rm bol}$ and the set of isochrones associated with the best fit model. Best fit parameters from the VOSA procedure are given in Table E.1. Fig. 4 shows $L_{\rm bol}$ and the ratio L_X/L_{bol} vs. $T_{\rm eff}$, where $L_{\rm bol}$ and $T_{\rm eff}$ have been obtained from the SED best fits. We observe that most of the members of the cluster are found between the isochrones of 5 and 10 Myr, with effective temperatures comprised in 3000-5500 K. The ages are in the range 2 – 90 Myr, with a 10% – 90% range of 3 – 18 Myr, these ages appear markedly older than the age of objects embedded in L1688. We will discuss the implications of the age difference in Sect. 4 The masses inferred from the fit to isochrones are in the range $0.1 - 1.2 M_{\odot}$, with a median of $0.45 M_{\odot}$.

3.3. X-ray spectral properties

For 27 bright X-ray sources with more than 500 counts in the combined EPIC image we performed a best fit modeling of their spectra with XSPEC (v 12.8). We adopted a combination of APEC thermal models plus absorption or an absorbed power law.

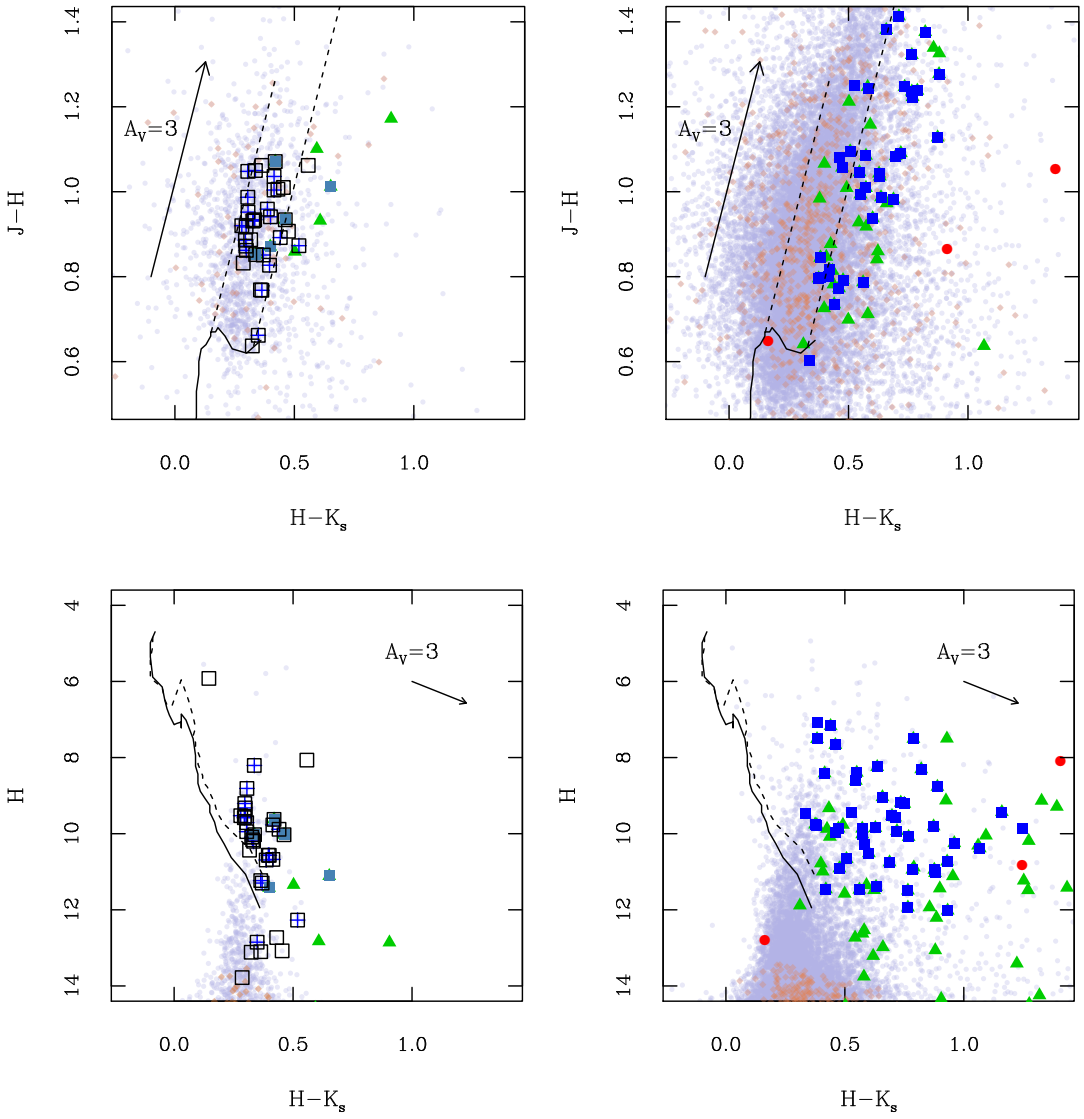

Fig. 3. Top panels: 2MASS $J-H$ vs. $H-K_s$ for objects around ρ Ophiuchi (left panel), and for L1688 (right panel). Bottom panels: H vs. $H-K_s$ for the same two regions. Isochrones at 10 Myr (solid line) and 5 Myr (dashed line) (Siess et al. 2000) at the distance of ρ Ophiuchi (120 pc) are traced in both panels. Symbols are as in Fig. 2. Reddening vectors corresponding to $A_V = 3$ are indicated. $A_V = 3$ is close to the extinction value derived from gas absorption N_H around ρ Ophiuchi, and this is about ten times lower than in L1688. An age comprised between 5 and 10 Myr for most of objects is also inferred from the best fit of $L_{\rm bol}$ and $T_{\rm eff}$ (Sect. 3.2).

The choice of the model has been driven by the source count statistics and the colors in the RGB image (see Fig. 1). In general for low count statistics faint sources with apparent hard X-ray spectrum we adopted a power law model, while for sources with softer spectra (hinting a spectrum from a stellar corona), we adopted a thermal model. The results are listed in Table D.1.

In star forming regions it has been observed that the ratio between gas absorption, probed by N_H, and dust extinction probed by A_V or A_K, is not constant. The difference could be ascribed to different grain size and flux ablation of grain surfaces in those regions with strong ambient UV flux from massive stars. To compare N_H and A_V we used a map of $E(B-V)$ (resolution $\sim$ 1.5′) based on IRAS and COBE/DIRBE data[2] (Schlafly & Finkbeiner 2011) to derive A_V by assuming an extinction law with $R_V = 3.1$. The average $E(B-V)$ is about 1.02 in the FOV of *XMM-Newton*, N_H values are found in a narrow range of values ($20.7 \leq \log N_{\rm H}({\rm cm}^{-2}) \leq 21.9$). N_H absorption appears is quite uniform across the FOV of *XMM-Newton*and sensibly lower, by a factor 5 to 10, than the values observed in the core F / L1688.

From the extinction map we derive an average A_V of 3.8 mag (10%-90% range: 3.6 – 4.1 mag) and a median N_H/A_V ratio of 1.04×10^{21} cm^{-2} mag^{-1}. The average N_H/A_V ratio near ρ Ophiuchi is lower than in Orion or the typical ISM value, and slightly higher than the values of N_H/A_V found in other low mass star forming regions like NGC 1333, Serpens and L1641 (Winston et al. 2007, 2010; Pillitteri et al. 2013). This evidence could be related to different amounts of ambient UV fluxes. High UV fluxes can ablate the surface of dust grains and hamper their growth modifying the overall properties of dust scattering. Another way to change the ratio is to selectively deplete the gas in

[2] irsa.ipac.caltech.edu/applications/DUST/

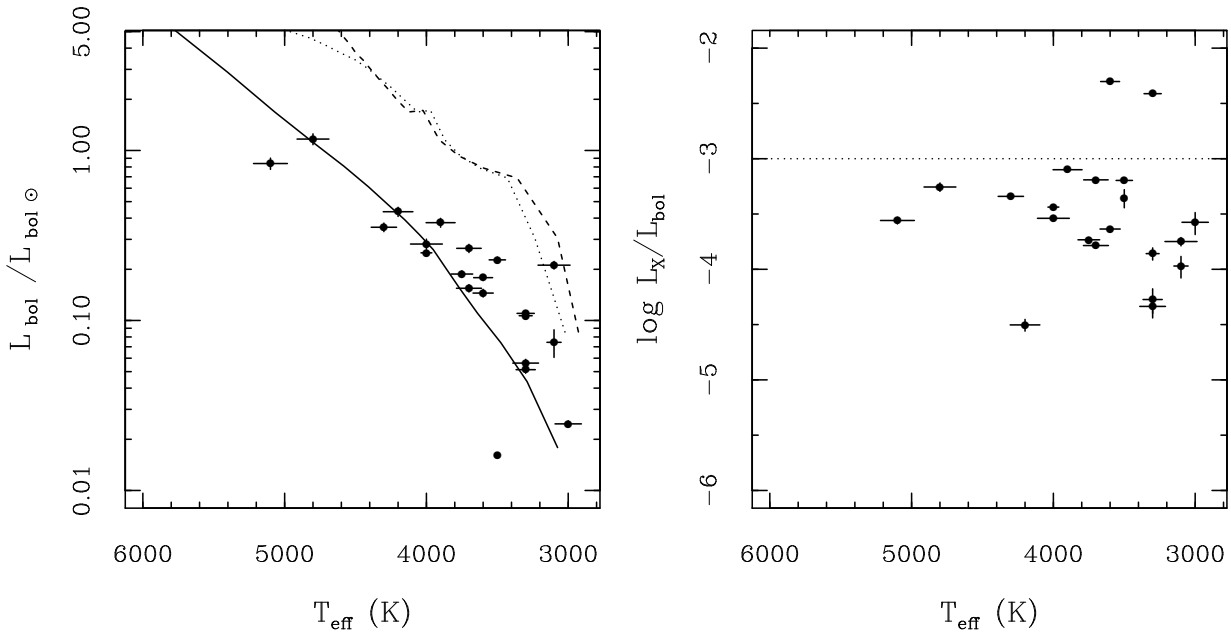

Fig. 4. Left: L_{bol} vs. $T_{\rm eff}$ for Class III stars and DDs in ρ Ophiuchi cluster with spectral fit to SEDs. Isochrones from Siess et al. (2000) at 1 Myr (dashed line), 5 Myr (dotted line) and 10 Myr (solid line) are traced. Most of the points are comprised betweeen 5 and 10 Myr isochrones. Right panel: $L_X/Lbol$ ratio vs. $T_{\rm eff}$ for YSOs in the ρ Ophiuchi cluster. Most of the objects lie below the saturation limit of $\log L_X/Lbol - 3$ (horizontal line), with the only exception of sources 1 and 61 which are found above it. The cause could be a systematic uncertainty by ~ 0.6 dex in $L_{\rm bol}$ or L_X. The points show an overall scatter of about 0.5 dex, and a slight decrease of the $L_X/Lbol$ ratio is visible for $T_{\rm eff} < 3500$.

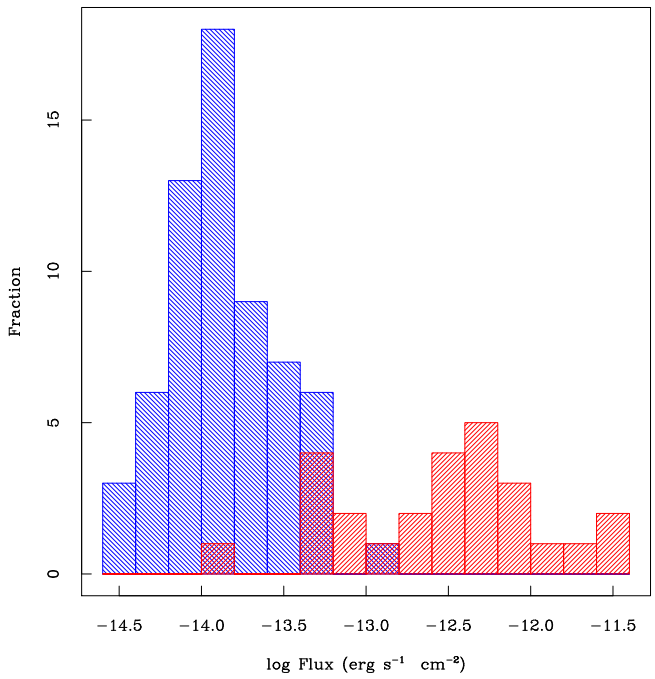

Fig. 5. Histogram of fluxes obtained from PIMMS (blue bars) and from spectral best fit (red bars).

favor of dust and this could be the mechanism at work in presence of stellar winds from B stars.

It is unlikely that the selection of bright X-ray sources for the spectral analysis could have introduced a bias toward sources at the surface of the cloud and thus with lower absorption. Hot young coronae at the distance of Rho Oph cloud and with plasma temperatures at $1 - 2$ keV, even when highly absorbed, are still bright enough above 1 keV, to have sufficient count statistics in a 50 ks *XMM-Newton* exposure. In this respect, we consider complete the bright sample and not biased toward sources with low absorption. The source with the lowest absorption is Src 79, it has no counterpart in 2MASS and its X-ray spectrum is best fitted with a power law of index $\alpha = 1.30 \pm 0.13$.

The range of plasma temperatures obtained from best fit to models with only one thermal APEC component is fairly limited: $kT = 0.24 - 1.7$ keV ($10\% - 90\%$), with mean of 1.1 keV. The best fits of models with two components give a mean second temperature of 1.7 keV, and those with 3 components give a mean third component of 3.2 keV. These values are in agreement with the temperatures of plasma in young coronae of other star forming regions.

3.4. X-ray luminosities

For the remaining 62 faint sources we derived a median energy from the distribution of source events and used PIMMS software to derive a flux assuming a thermal APEC model with only one component. For N_H we used a weighted mean of the N_H values from the best fit to spectra of the bright sources, with the weight being the inverse of the spatial distance to the positions of sources in the bright sample. This approach is almost equivalent to considering an unique value taken from the average N_H, given that the absorption is quite uniform across the FOV of *XMM-Newton* and small variations are expected from source to source. Fig. 5 shows the histogram of fluxes derived from PIMMS (green) and from XSPEC (red) for all X-ray sources. The range is in $-14.56 < \log f_X < -11.5$. Errors in fluxes from PIMMS can be derived from the uncertainties in count rates; systematic errors due to a different plasma temperature can amount

to about 10% for temperatures in 0.5 – 2 keV. The relative errors of PIMMS fluxes have a median of ∼ 17%, and a 25% – 75% quantile range of 8% – 24%. For XSPEC derived fluxes, these have relative errors with a median of 3.5% and a 25% – 75% quantile range of 2% – 8%. At the distance of ρ Ophiuchi the minimum detected flux corresponds to $\log L_X \sim 27.7$. Assuming a complete detection above $\log L_X \sim 28$ and a saturated L_X/L_{bol} ratio, this would imply a detection of YSOs with $L_{bol} \sim 10^{32}$ erg s^{-1} $\sim 0.1 L_{bol\odot}$. This is approximately the luminosity of stars of M3-M4 spectral type at 5 Myr (Siess et al. 2000), which represent the low mass limit of the X-ray detections, although we presume that we have completeness only at late K- / early M-types.

The ratio L_X/L_{bol} (Fig. 4, right panel) shows a dynamical range of three orders of magnitude. The cluster members are distributed in a sequence of values that goes from ρ Ophiuchi A+B and ρ Ophiuchi C ($L_X/L_{bol} = 2\times10^{-6}$ and 4×10^{-5}, respectively) to cooler objects which ratios peak at around 10^{-3}, a value found among the most active and young coronae (Caillault & Helfand 1985; Micela et al. 1985; Stauffer et al. 1994). The origin of this value is debated but it could be a limit to the efficiency in the production of X-rays in dynamo driven coronae of active stars (Charbonneau & MacGregor 1992) or a breaking of magnetic loops in fast rotating stars (Jardine & Unruh 1999).

Fig. 6 shows the distribution of X-ray luminosities of Class III stars earlier than M5 around ρ Ophiuchi and the analog curves of stars in L1688 (from DROXO; Pillitteri et al. 2010), and from L1641 (Pillitteri et al. 2013). For L1688 we report the total and a *corrected* distribution after removing some suspicious members from the list of Bontemps et al. (2001), mostly upper limits to luminosity. Given the deep sensitivity of DROXO, it is quite unlikely that Class III stars remain undetected and thus the corrected distribution is more reliable than the distribution of the full sample. The three distributions tend to be similar, with a slight under luminosity of the group of stars around ρ Ophiuchi for values below $\log L_X \sim 29.5$. In ONC the X-ray luminosities of non accreting stars in the range of mass 0.3 – 1.0 $M_\odot$ have values around $\log L_X \sim 29 - 29.5$ erg/s (Preibisch et al. 2005), and similar values are found in Taurus Molecular Cloud (Güdel & Telleschi 2007). Another small difference is the standard deviation of $\log L_X$ is 0.74 dex for Rho Oph, 0.69 dex in L1688 and 0.59 dex in L1641. Similar differences are found in Classical versus Weak T-Tauri stars (Telleschi et al. 2007). However, this effect is minor when comparing entire populations (Kuhn et al. 2015; Feigelson et al. 2011) and cannot rule out the hypothesis of an *universal* X-ray luminosity function for PMS stars as proposed by Feigelson et al. (2005).

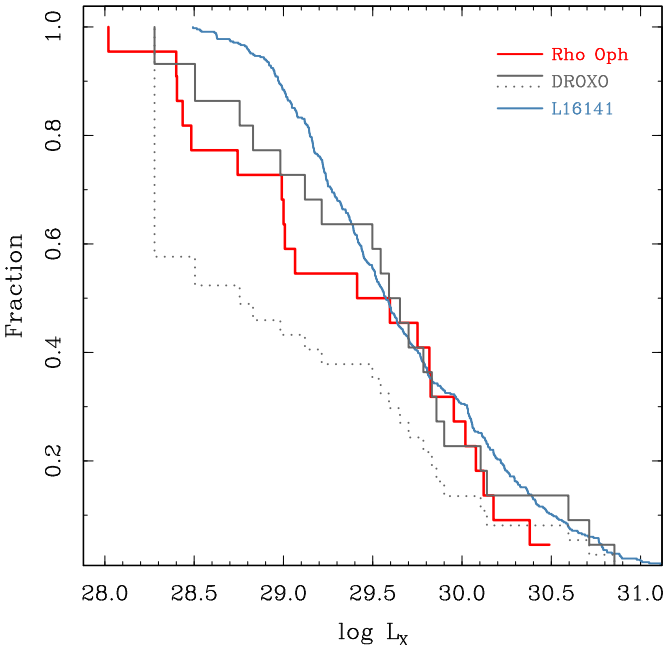

Fig. 6. X-ray luminosity function of Class III stars (comprised 3 DDs). For comparison we added the curves of Class III stars in L1688 from DROXO, both corrected (solid gray line) and total sample (dotted gray line, see Pillitteri et al. 2010), and L1641 (solid light blue line, Pillitteri et al. 2013). Class III stars around ρ Ophiuchi shows less luminosities and a larger range of values.

Table 2. Best fit parameters of the spectral analysis of ρ Ophiuchi C. The models are 2T APEC plus global absorption. The non flaring intervals are approximately the first 8 ks and the interval after the second flare (see Fig. F.1.

Intervals:	Quiescent	Flare 1	Flare 2
N_H (cm^{-2})	0.38 ± 0.02	0.42 ± 0.03	0.41 ± 0.03
kT_1 (keV)	1.01 ± 0.02	0.97 ± 0.05	1.02 ± 0.04
$Z/Z_\odot$	0.11 ± 0.02	0.35 ± 0.11	0.35 ± 0.13
$N_1(10^{-4}$ cm$^{-5})$	16.8 ± 2.4	6.7 ± 2.5	8 ± 3
kT_2 (keV)	3.7 ± 0.6	2.9 ± 0.2	3.0 ± 0.4
$N_2(10^{-4}$ cm$^{-5})$	5.1 ± 0.9	13.6 ± 1	10.4 ± 1.1
Flux (10^{-12} erg s^{-1} cm^{-2})	1.96	2.7	2.43
χ^2	156.7	134.3	65.7
Degrees of freedom	160	89	79

3.5. X-ray variability

Strong X-ray variability is detected in several sources. Light curves of the brightest sources are shown in Appendix (Fig. F.1). Here we detail the most prominent cases.

3.5.1. ρ Ophiuchi A+B

Variable X-ray emission from the ρ Ophiuchi A+B system has been detected, this variability has been studied in details and published in a separate paper (Pillitteri et al. 2014). Briefly, smooth variability was observed in ρ Ophiuchi on a time scale of 10 ks. The flux has a low state in the first 30 ks of observation, a slow rise for about 10 ks, and a high state for the rest of the observation, with a component of $kT \sim 3.0$ keV gradually appearing in the spectrum during the rise. The interpretations is that a hot spot of magnetic origin appears on the visible face of the primary star because of the stellar rotation (≥ 300 km/s). We inferred a size of the spot of about half of the stellar radius if the spot is at the equator. The magnetic origin of this spot is interesting given so few cases of magnetic B2 stars known in literature. In this respect, ρ Ophiuchi is likely the best target where to investigate the origin of magnetic fields in massive stars due to its proximity.

3.5.2. ρ Ophiuchi C

ρ Ophiuchi C (HD 147932, source nr. 62) is composed by a B5 type star (V = 5.8 mag) and a low mass companion (V = 11.7, Mason et al. 2001). Recently, it has been discovered that the primary possesses an intense magnetic field (> 3000 G, Alecian et al. 2014). This star has a peculiar optical spectrum with weak

He I lines. It is a fast rotator, with vsin $i \sim 140$ km/s, and displays changes in the spectra taken one night apart. These changes can be ascribed to rotational features.

ρ Ophiuchi C exhibited two bright flares with very similar peak intensities and decay times (see curve of Src. 62 of Fig. F.1 in Appendix). Other modulated emission is also recognized. The decay time of both flares is approximately 4 ks, with the quiescent level reached at ∼20 ks for the first flare and at ∼ 31 ks for the second flare. Table 2 reports the best fit results of modeling the spectra during the flares and during the quiescent state, which has a best fit with a combination of two absorbed APEC thermal components. We have tested to model the flaring spectra with three components, keeping two components fixed to the quiescent best fit model, however the fit gave an unrealistically high temperature with a negligible component normalization. On the other hand, models with two thermal components gave a good fit for the flare spectra. In this case, the hot component of the two flaring spectra was found similar to the hot component of the spectrum post-flares, albeit with a normalization larger by one order of magnitude.

Modeling of magnetically confined plasma in solar coronal loops has been extensively studied by Reale (2007) in order to develop diagnostics for stellar flares. We can apply this modeling to the flare light curve in order to derive a loop length, by taking into account the rise and decay times (1.8 ks and 10 ks, respectively) and the peak plasma temperature derived from the flaring intervals in Table 2. Using eq. 12) in Reale (2007), we find a loop semi-length of $\sim 4 \times 10^{10}$ cm for both flares. It is unclear which star of the ρ Ophiuchi C system flared. Young K type stars have enhanced variability and do flare more often than B late type stars (Pye et al. 2015). The companion of ρ Ophiuchi C is a late K type star ($V = 11.7$) at an age of ~ 5 Myr and it is expected to be very active and variable in X-rays. Given these characteristics it is plausible that this star hosted both flares. The loop semi-length of both flares would be comparable with the stellar radius. Were the flares generated in a magnetized corona of the B7 primary, this would be among the few examples of flare-like variability detected in a B late type star.

3.5.3. Other variable sources

In addition to ρ Ophiuchi C, we find impulsive variability in sources nr. 10, 38 and 41. Sources 17, 20, 31, 71, 83, and 84 show less identifiable variability. In source 84 we see an overall decrease of the flux as if it is part of the decay of a long lasting flare. Some minor flickering at level of 2 σ significance is over imposed to the global trend.

Among the flaring sources 10, 38 and 41, the latter is flaring at the beginning of the observation for $t < 10$ ks. The subsequent portion of light curve shows some slow decrease after minor impulses. We have analyzed the spectra of the main flare and of the post-flaring intervals. The best fit model of the post flare spectrum was given by sum of two APEC thin plasma models absorbed by a common N_H column. The two temperatures were $kT_1 = 0.93 \pm 0.04$ keV, $kT_1 = 2.2 \pm 0.2$, the normalization factors were $N_1 = (7.2 \pm 1) \times 10^{-5}$ cm^{-5} and $N_2 = (9.3 \pm 1.1) \times 10^{-5}$ cm^{-5}; the absorption was $N_H = (2.0 \pm 0.3) \times 10^{21}$ cm^{-2}. For the flare, we used a 3T APEC model with the first two components fixed to the post flare best fit model. In this case, the third thermal component had a best fit value of $kT = 2.5 \pm 0.3$ keV and normalization $N_3 = (2,3 \pm 0.2) \times 10^{-4}$ cm^{-5}, i.e., a factor 2 to 2.8 higher than the thermal components of the post-flare spectrum. By using the scaling laws of Reale (2007) and Serio et al. (1991) as in the case of ρ Ophiuchi C, we estimate a loop semi-length of $l \geq 5.8 \times 10^{10}$ cm or 0.8 $R_\odot$. This is a lower limit given that we did not observe the rise and the peak of the flare. The post flare spectrum appears somewhat hot, and that could be over dense plasma flared loop still cooling down after the fast decay happened during the first 10 ks of observation. We speculate that the small secondary impulses seen in the light curve could have been triggered by the main flare as observed in the Sun in complex active regions (e.g. Aschwanden & Alexander 2001).

4. Discussion

The first issue we discuss is the comparison between ρ Ophiuchi cluster and YSOs in L1688. We have shown that there is a cluster of about 28 YSOs surrounding ρ Ophiuchi and born from the same natal cloud. There is evidence of a significant age difference between this cluster and the YSOs in L1688. The first evidence is pointed out by the comparison of the number of stars with disks and stars without disks in the two regions inferred from WISE and 2MASS photometry and joint IR/X-ray classification. The ratio of disks/no-disks objects is a statistical probe of the evolutionary status of star formation in the cloud and ultimately of the stellar ages (see Haisch et al. 2001; Strom 1995). We count 22 disk-less stars, 3 DD objects and three stars with disks (but two stars with disks are at the very edge of the *XMM-Newton* FOV, see Fig. 7) near ρ Ophiuchi, giving thus a frequency of disks of about 1:8, which is similar to what observed with ROSAT (Martin et al. 1998). One protostar/Class I object is at the very edge of *XMM-Newton* FOV and it is undetected, another Class I object is Haro 1-4 which is detected. In contrast, L1688 core contains a significant number of stars with disks and protostars embedded in the densest part of the cloud (Gagné et al. 2004), and the ratio stars with disks to disk-less stars is of order of 1 or more. The age inferred from the ratio disks/no-disk objects around ρ Ophiuchi is about 5 Myr, while for L1688 embedded YSOs an age $t < 1$ Myr is inferred (Luhman & Rieke 1999; Natta et al. 2002). Other evidence of ages around $5 - 10$ Myr near ρ Ophiuchi is given by the 2MASS color-magnitude diagrams and model isochrones at 5 Myr and 10 Myr, and by the HR diagram obtained from SEDs modeling and fitting to isochrones (Sect. 3.2). We can firmly conclude that around ρ Ophiuchi there is a small cluster a factor of 5 to 10 older than the age of YSOs in the L1688 core.

Wilking et al. (2005) analyzed optical spectra from the surface population surrounding L1688, deriving spectral types, temperatures, masses and ages for their sample. The objects in Wilking et al. (2005) have temperatures in the range $2500 - 19,000$ K, with a mean $T_{\rm eff}$ of 3350 K and 90% quantile at 4380 K. This range of $T_{\rm eff}$ values is similar to the range we find from SED analysys. There is a similar concurrence among the masses derived by Wilking et al. (range: $0.14 \leq M/M_\odot \leq 0.82$, mean: $0.22 M_\odot$).

The ages inferred by Wilking et al. (2005) have a peak at $t = 2.1$ Myr ($10\% - \%90$ quantiles range: $0.5 \leq t \leq 8.2$ Myr). As first hypothesized by Wilking et al., the stars clustered around ρ Ophiuchi were formed in a early episode of star formation in the cloud, about $4-5$ Myr ago. We also speculate that the densest part cloud was larger in the past and that a fraction of the stars have since migrated away from the cloud. What we observe now is the patchy "left-over" cloud of a process of star formation that did not occurred uniformly across the cloud. The group of disk-less stars we found in X-rays around ρ Ophiuchi constitute an early product of that star forming burst. These stars appear to share similar proper motions (Fig. 7), roughly moving toward north west at 100 mas yr^{-1}. On the other hand, the few Class I

and II YSOs around ρ Ophiuchi show larger proper motions and could have traveled into the region coming from the denser core of L1688.

The Dark Cloud of ρ Ophiuchi appears to be related to two other nearby star forming regions, namely Upper Sco-Cen and Upper Centaurus-Lupus. These also contain YSOs older than L1688. Preibisch & Zinnecker (1999) suggested that star formation has proceeded starting from Upper Centaurus-Lupus 5 Myr ago, then triggered Upper Sco-Cen about 4 Myr ago. About 1.5 Myr ago a supernova explosion eventually created the runaway star ζ Oph, and the same blast triggered star formation in Rho Oph about 1 Myr ago. Our results challenge this scenario. In the north-western edge of L1688 core, star formation has started earlier than 1 Myr ago, likely 5 Myr ago, and the "Real Rho Oph cluster" appears coeval to Upper Sco-Cen and Upper Centaurus-Lupus. The massive stars of the ρ Ophiuchi systems were formed along with other $\geq$ 25 solar and sub-solar mass stars north west of L1688. Eventually the dust and gas in this part of the cloud has been dispersed by the collective action of stellar winds from the massive stars in it. While it is not ruled out a triggering of star formation due to the progenitor of ζ Oph, this can not have been the solely mechanism of star formation directly associated with Rho Oph. In our scenario it may be possible that ρ Ophiuchi had a role in triggering the star formation also in L1688 at a later phase.

The total X-ray luminosity of the ρ Ophiuchi cluster amounts to at least $\sim 5.6 \times 10^{30}$ erg s^{-1}. If this is the minimum rate of emission during a lifetime of $t = 3 - 5$ Myr, at least 5×10^{44} erg in X-ray band have been injected into the surrounding cloud. If we assume that the stars have a saturated $L_X/L_{bol} \simeq 10^{-3}$, the total energy deposited into the cloud during the stellar lifetime is up to $\leq 10^{47}$ erg. Chen et al. (in prep.) estimated the total cloud mass (about $\sim 3.37 \times 10^3 M_\odot$), energy and velocity of the expanding bubble around ρ Ophiuchi. The kinetic energy of the bubble is about 6.7^{45} erg, the expansion velocity is $\sim$ 1.3 km/s and the time to inflate the bubble (which size is about 1.36 pc) is $\sim$ 1.2 Myr. The energy entrained in the cloud can be consistent with the energy radiated by the young stars within the bubble, with an efficiency factor of $10 - 15\%$ for converting radiated energy into kinetic energy of the bubble. However, the age of the bubble appears too short when compared to the age of stars in it and this remains an open issue in the connection between stars and natal cloud. It is also worth noticing that Chen et al. assumed a constant expansion velocity of the shell throughout the lifetime of the shell. While this is generally true for the snowplow phase (i.e. when the bubble has expanded beyond the densest part of the cloud), the initial expansion velocity could be slower due to the dense material surrounding the young stars when they were born. Chen et al. noted that the estimate of the shell formation timescale of 1.2 Myr could be a lower bound. We speculate that the efficiency in transferring energy to the cloud in form of kinetic energy was lower during the very early phases of star formation, when the gas of the cloud was denser, this effectively delaying the time of inflation of the bubble.

5. Conclusions

We have presented the analysis of an *XMM-Newton* observation of 53 ks centered on the ρ Ophiuchi A+B system. We found a total of 89 X-rays sources, 47 of them with WISE counterparts. We have classified them according to their WISE colors and magnitudes and used X-ray detection as a further criterion to classify disk-less stars bright in X-rays. In this way we identified a group of 22 young disk-less stars surrounding ρ Ophiuchi. These stars

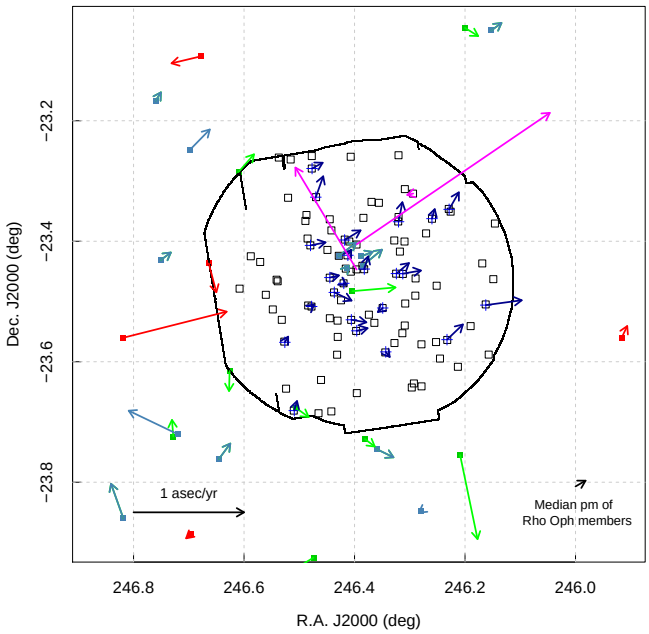

Fig. 7. Spatial distribution of the X-ray sources (open squares) and YSOs (crosses and filled colored symbols) in the *XMM-Newton* FOV with their proper motions (arrows). Magenta arrows are for ρ Ophiuchi A+B, ρ Ophiuchi C and Haro 1-4 stars. Red are Class I YSOs, green are Class II YSOs, blue are Class III stars. These latter share similar proper motions and form a cluster about 5 Myr old formed *in situ*, while Class I and Class II YSOs seem to have larger proper motions and have traveled across the FOV of *XMM-Newton*. The large proper motions of ρ Ophiuchi A+B and ρ Ophiuchi C are likely related to their binarity nature.

constitute a small cluster formed about 5 to 10 Myr ago during a previous event of star formation just north of L1688 dense core of the cloud. Another indicator of age is the almost absence of stars with disks in the *XMM-Newton* FOV. In fact, only three Transition Disk / Debris Disk objects are found in it, adding thus evidence of a more evolved stage of star formation in the region with respect to the core of L1688 with younger YSOs ($t \sim 1$ Myr). This cluster, older than the average age of the well studied L1688 core of the cloud, challenges the scenario of triggered star formation in Upper Sco-Cen and Rho Oph proposed by Preibisch & Zinnecker (1999). In particular, it is evident that star formation has started in the cloud about 5 Myr ago simultaneously with Upper Sco-Cen and Upper Centaurus Lupus. Thus YSOs in Rho Oph cloud are not the solely result of the sweeping action and triggered star formation due to super novae explosions happened in Upper Sco-Cen as proposed by Preibisch & Zinnecker (1999)

The energy radiated from the stars into the interstellar medium is sufficient to inflate the observed bubble, however the time to form the bubble is about five times shorter than the age of the stars in it. To solve the issue, we could speculate of a lower efficiency of transformation of the energy radiated from stars into kinetic energy the cloud in the early phases that delayed the inflation of the bubble.

Some stars exhibit variability in form of flares or in less classifiable shape. The flaring rate appears lower than in the core F of L1688. Time resolved spectroscopy of the most intense flares

lead to estimate loop lengths of order of the stellar radius, which are compatible with similar findings in other young active stars.

References

Alecian, E., Kochukhov, O., Petit, V., et al. 2014, A&A, 567, A28
Allard, F., Hauschildt, P. H., Alexander, D. R., Tamanai, A., & Schweitzer, A. 2001, ApJ, 556, 357
Allard, F., Homeier, D., & Freytag, B. 2012, Royal Society of London Philosophical Transactions Series A, 370, 2765
Arce, H. G., Borkin, M. A., Goodman, A. A., Pineda, J. E., & Beaumont, C. N. 2011, ApJ, 742, 105
Arnaud, K., Dorman, B., & Gordon, C. 1999, in Astrophysics Source Code Library, record ascl:9910.005, 10005
Aschwanden, M. J. & Alexander, D. 2001, Sol. Phys., 204, 91
Baraffe, I., Chabrier, G., Barman, T. S., Allard, F., & Hauschildt, P. H. 2003, A&A, 402, 701
Bayo, A., Rodrigo, C., Barrado Y Navascués, D., et al. 2008, A&A, 492, 277
Bontemps, S., André, P., Kaas, A. A., et al. 2001, A&A, 372, 173
Caillault, J. . & Helfand, D. J. 1985, ApJ, 289, 279
Casanova, S., Montmerle, T., Feigelson, E. D., & Andre, P. 1995, ApJ, 439, 752
Chabrier, G., Baraffe, I., Allard, F., & Hauschildt, P. 2000, ApJ, 542, 464
Charbonneau, P. & MacGregor, K. B. 1992, ApJ, 387, 639
Churchwell, E., Povich, M. S., Allen, D., et al. 2006, ApJ, 649, 759
Damiani, F., Maggio, A., Micela, G., & Sciortino, S. 1997a, ApJ, 483, 350
Damiani, F., Maggio, A., Micela, G., & Sciortino, S. 1997b, ApJ, 483, 370
Elmegreen, B. G. 1998, in Astronomical Society of the Pacific Conference Series, Vol. 148, Origins, ed. C. E. Woodward, J. M. Shull, & H. A. Thronson, Jr., 150
Evans, II, N. J., Allen, L. E., Blake, G. A., et al. 2003, PASP, 115, 965
Feigelson, E. D., Getman, K., Townsley, L., et al. 2005, ApJS, 160, 379
Feigelson, E. D., Getman, K. V., Townsley, L. K., et al. 2011, ApJS, 194, 9
Flaccomio, E., Stelzer, B., Sciortino, S., et al. 2009, A&A, 505, 695
Gagné, M., Fehon, G., Savoy, M. R., et al. 2011, ApJS, 194, 5
Gagné, M., Skinner, S. L., & Daniel, K. J. 2004, ApJ, 613, 393
Getman, K. V., Broos, P. S., Feigelson, E. D., et al. 2011, ApJS, 194, 3
Giardino, G., Favata, F., Pillitteri, I., et al. 2007, A&A, 475, 891
Güdel, M. & Telleschi, A. 2007, A&A, 474, L25
Gutermuth, R. A., Megeath, S. T., Myers, P. C., et al. 2009, ApJS, 184, 18
Gutermuth, R. A., Pipher, J. L., Megeath, S. T., et al. 2011, ApJ, 739, 84
Haisch, Jr., K. E., Lada, E. A., & Lada, C. J. 2001, ApJ, 553, L153
Imanishi, K., Tsujimoto, M., & Koyama, K. 2001, ApJ, 563, 361
Jardine, M. & Unruh, Y. C. 1999, A&A, 346, 883
Koenig, X. P. & Leisawitz, D. T. 2014, ApJ, 791, 131
Kryukova, E., Megeath, S. T., Gutermuth, R. A., et al. 2012, AJ, 144, 31
Kuhn, M. A., Feigelson, E. D., Getman, K. V., et al. 2015, ApJ, 812, 131
Lada, C. J. & Adams, F. C. 1992, ApJ, 393, 278
Loinard, L., Torres, R. M., Mioduszewski, A. J., & Rodríguez, L. F. 2008, ApJ, 675, L29
Luhman, K. L. & Rieke, G. H. 1999, ApJ, 525, 440
Maheswar, G., Manoj, P., & Bhatt, H. C. 2003, A&A, 402, 963
Martin, E. L., Montmerle, T., Gregorio-Hetem, J., & Casanova, S. 1998, MNRAS, 300, 733
Mason, B. D., Wycoff, G. L., Hartkopf, W. I., Douglass, G. G., & Worley, C. E. 2001, AJ, 122, 3466
Micela, G., Sciortino, S., Serio, S., et al. 1985, ApJ, 292, 172
Montmerle, T., Koch-Miramond, L., Falgarone, E., & Grindlay, J. E. 1983, ApJ, 269, 182
Natta, A., Testi, L., Comerón, F., et al. 2002, A&A, 393, 597
Ozawa, H., Grosso, N., & Montmerle, T. 2005, A&A, 438, 661
Pillitteri, I., Sciortino, S., Flaccomio, E., et al. 2010, A&A, 519, A34
Pillitteri, I., Wolk, S. J., Goodman, A., & Sciortino, S. 2014, A&A, 567, L4
Pillitteri, I., Wolk, S. J., Megeath, S. T., et al. 2013, ApJ, 768, 99
Preibisch, T., Kim, Y.-C., Favata, F., et al. 2005, ApJS, 160, 401
Preibisch, T. & Zinnecker, H. 1999, AJ, 117, 2381
Pye, J. P., Rosen, S., Fyfe, D., & Schroeder, A. C. 2015, ArXiv e-prints
Reale, F. 2007, A&A, 471, 271
Schlafly, E. & Finkbeiner, D. P. 2011, in Bulletin of the American Astronomical Society, Vol. 43, American Astronomical Society Meeting Abstracts #217, 434.42
Schnee, S. L., Ridge, N. A., Goodman, A. A., & Li, J. G. 2005, ApJ, 634, 442
Serio, S., Reale, F., Jakimiec, J., Sylwester, B., & Sylwester, J. 1991, A&A, 241, 197
Siess, L., Dufour, E., & Forestini, M. 2000, A&A, 358, 593
Snowden, S. L. 1994, in Bulletin of the American Astronomical Society, Vol. 26, American Astronomical Society Meeting Abstracts #184, 940
Stauffer, J. R., Caillault, J.-P., Gagnè, M., Prosser, C. F., & Hartmann, L. W. 1994, ApJS, 91, 625
Strom, S. E. 1995, in Revista Mexicana de Astronomia y Astrofisica Conference Series, Vol. 1, Revista Mexicana de Astronomia y Astrofisica Conference Series, ed. S. Lizano & J. M. Torrelles, 317
Telleschi, A., Güdel, M., Briggs, K. R., Audard, M., & Palla, F. 2007, A&A, 468, 425
Townsley, L. K., Broos, P. S., Corcoran, M. F., et al. 2011, ApJS, 194, 1
Wilking, B. A., Gagné, M., & Allen, L. E. 2008, Star Formation in the ρ Ophiuchi Molecular Cloud, ed. B. Reipurth, 351–+
Wilking, B. A., Meyer, M. R., Robinson, J. G., & Greene, T. P. 2005, AJ, 130, 1733
Winston, E., Megeath, S. T., Wolk, S. J., et al. 2007, ApJ, 669, 493
Winston, E., Megeath, S. T., Wolk, S. J., et al. 2010, AJ, 140, 266
Wright, E. L., Eisenhardt, P. R. M., Mainzer, A. K., et al. 2010, AJ, 140, 1868

Acknowledgements. I.P. is thankful to Dr. Mario Guarcello for the fruitful discussions about the lifetime and evaporation of circumstellar disks in PMS stars. S.J.W. was supported by NASA contract NAS8-03060. This publication makes use of VOSA, developed under the Spanish Virtual Observatory project supported from the Spanish MICINN through grant AyA2011-24052. Based on observations obtained with XMM-Newton, an ESA science mission with instruments and contributions directly funded by ESA Member States and NASA.

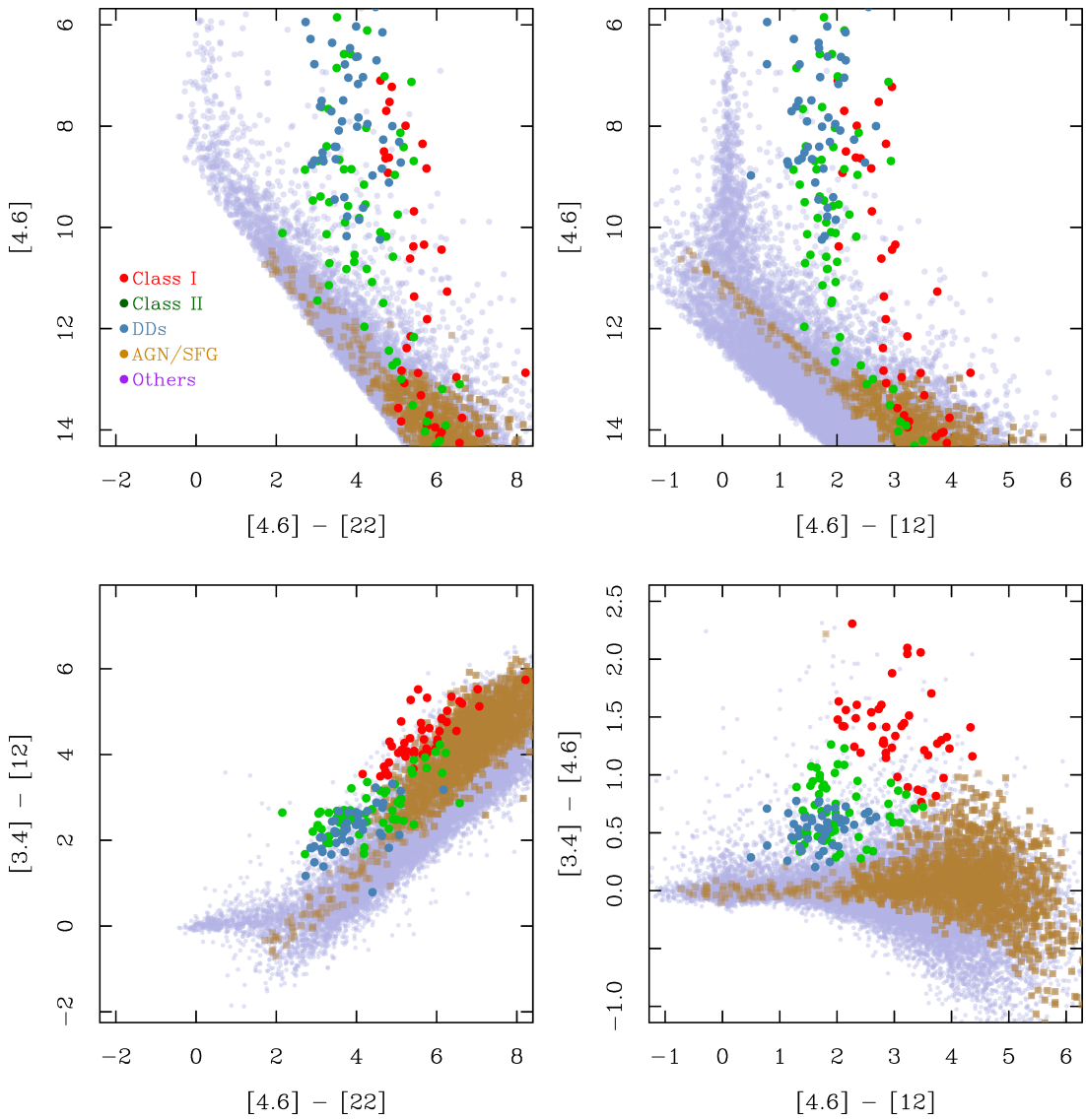

Fig. A.1. Same as in Fig. 2 for objects in L1688 within 1 deg from SR 12A. Differently from ρ Ophiuchi region, we find many Class I and Class II YSOs.

Appendix A: WISE diagrams of L1688.

Appendix B: List of X-ray sources

Appendix C: List of IR counterparts

Appendix D: Parameters of best fit modeling of X-ray spectra

Appendix E: Results from best fit to SEDs

Appendix F: Light curves

Table B.1. Properties of X-ray sources. Coordinates, positional errors, off-axis angle, exposure time, count rates, errors on count rates and significance are listed. Flags indicating the classification based on IR/X-ray emission (see Sect. 3.1) are also indicated.

	RA	Dec	Pos.Err	Offaxis	Exp.time	Count.rate	Err.Rate	Significance	Flux		RA	Dec	Pos.Err	Offaxis	Exp.time	Count.rate	Err.Rate	Significance	Flux
	Deg (J2000)	Deg. (J2000)	arcmin	ks	ct ks^{-1}	ct ks^{-1}	ct ks^{-1}	σ	10^{-14}erg s^{-1} cm^{-2}		Deg (J2000)	Deg. (J2000)	arcmin	ks	ct ks^{-1}	ct ks^{-1}	ct ks^{-1}	σ	10^{-14}erg s^{-1} cm^{-2}
1	246.50999	-23.68115	2.1	13.16	26.83	66.2	2.0	60.5	87.1	46	246.44489	-23.46047	1.8	3.71	117.72	6.0	0.3	40.2	60.6
2	246.39589	-23.65206	3.5	9.57	55.26	1.4	0.2	8.1	2.0	47	246.31255	-23.45428	3.0	4.72	134.83	0.4	0.1	5.8	0.6
3	246.52393	-23.64472	2.7	11.81	51.61	1.1	0.2	7.4	1.6	48	246.32470	-23.45381	1.2	4.17	134.06	31.5	0.6	122.2	32.7
4	246.29637	-23.64279	5.0	10.30	32.22	3.2	0.6	9.4	4.6	49	246.40655	-23.45051	1.8	2.75	131.16	0.2	0.1	4.9	0.4
5	246.27875	-23.64088	4.1	10.71	56.08	0.8	0.2	5.0	1.3	50	246.39647	-23.44674	0.8	2.81	133.25	141.8	1.0	280.0	300.0
6	246.29254	-23.63603	2.4	10.05	57.04	1.3	0.2	9.2	1.9	51	246.38253	-23.44644	1.8	2.79	134.36	1.8	0.2	19.9	3.2
7	246.46064	-23.63028	3.3	9.18	53.10	7.1	0.6	23.1	10.2	52	246.41584	-23.44544	2.4	3.25	99.95	3.7	0.3	26.3	9.0
8	246.21291	-23.60839	4.8	11.84	66.90	1.6	0.3	8.6	2.4	53	246.38580	-23.44071	2.5	3.13	135.86	0.8	0.1	8.7	1.4
9	246.24531	-23.59472	4.5	9.92	78.63	1.6	0.2	9.3	2.4	54	246.16879	-23.43680	1.9	12.49	51.91	20.3	1.0	50.6	45.1
10	246.43154	-23.58834	3.4	6.23	72.43	1.0	0.2	9.1	1.4	55	246.57079	-23.43441	3.9	10.69	60.48	1.0	0.2	6.8	1.5
11	246.15713	-23.58815	3.3	13.90	26.45	3.6	0.6	11.9	5.4	56	246.58780	-23.42495	4.8	11.76	52.22	2.1	0.3	8.7	3.2
12	246.34435	-23.58452	2.1	5.99	81.44	18.6	0.6	60.3	5.7	57	246.42853	-23.42416	2.8	4.70	105.61	1.5	0.2	13.2	3.0
13	246.27888	-23.57108	2.8	7.59	77.09	0.5	0.1	6.8	0.8	58	246.41281	-23.42343	2.9	4.39	116.65	1.3	0.2	11.8	5.9
14	246.32773	-23.56896	4.2	5.63	85.76	0.5	0.1	4.7	0.7	59	246.31788	-23.41718	3.1	5.93	126.73	0.3	0.1	4.9	0.5
15	246.25247	-23.56733	2.6	8.66	82.91	0.6	0.1	7.0	1.0	60	246.44906	-23.41442	2.5	5.80	108.13	0.6	0.1	8.6	1.0
16	246.52719	-23.56657	5.7	8.87	69.22	1.0	0.2	5.4	1.5	61	246.47999	-23.40686	0.9	7.25	87.82	133.4	2.0	212.0	139.0
17	246.23220	-23.56384	1.9	9.54	84.01	34.0	0.9	91.8	38.7	62	246.39643	-23.40545	0.8	5.27	118.52	159.6	2.0	278.4	306.0
18	246.43039	-23.55880	2.2	4.61	105.31	1.0	0.1	12.6	1.4	63	246.30951	-23.40045	2.3	7.01	112.75	0.2	0.1	4.8	0.3
19	246.31344	-23.55269	3.1	5.43	59.90	0.3	0.2	4.7	0.5	64	246.40947	-23.40044	3.2	5.67	116.22	0.4	0.1	4.6	0.7
20	246.39709	-23.54892	1.3	3.41	86.99	41.2	1.0	118.0	50.0	65	246.32809	-23.39869	4.9	6.52	118.89	0.8	0.1	7.3	1.4
21	246.18988	-23.54087	5.8	11.24	76.65	0.8	0.2	5.8	1.2	66	246.41772	-23.39724	3.6	5.97	107.07	0.8	0.1	6.9	1.6
22	246.30907	-23.53986	4.2	5.15	113.65	0.4	0.1	4.9	0.6	67	246.48503	-23.39551	3.3	7.94	66.60	1.7	0.3	10.2	2.6
23	246.36410	-23.53545	3.0	2.86	127.22	1.0	0.1	12.0	1.4	68	246.27048	-23.38697	2.9	9.04	100.94	0.4	0.1	6.1	0.7
24	246.43070	-23.53176	4.1	3.34	115.46	0.4	0.1	5.5	0.6	69	246.44187	-23.38201	3.5	7.29	76.35	1.0	0.2	7.9	1.5
25	246.53167	-23.53044	3.6	8.25	58.43	0.5	0.2	4.8	0.9	70	246.14586	-23.37060	3.1	15.18	24.49	1.6	0.4	7.5	2.4
26	246.40614	-23.53050	1.8	2.49	123.29	5.8	0.3	41.5	6.7	71	246.32095	-23.36722	1.3	8.38	68.47	40.8	1.0	100.1	69.4
27	246.44470	-23.52781	3.3	3.79	111.57	0.9	0.1	9.4	1.3	72	246.48893	-23.36626	3.9	9.43	60.17	3.1	0.3	13.5	5.9
28	246.37404	-23.52188	3.8	1.89	132.70	0.5	0.1	6.2	0.6	73	246.44889	-23.36354	3.1	8.38	69.64	0.5	0.1	4.8	0.7
29	246.54793	-23.51319	4.4	8.92	70.22	1.9	0.3	10.4	2.9	74	246.25978	-23.36266	1.9	10.50	74.34	8.3	0.5	37.0	15.0
30	246.34917	-23.51089	1.9	2.37	136.95	4.2	0.2	35.8	5.8	75	246.38395	-23.36119	5.5	7.90	77.97	0.9	0.2	5.5	1.4
31	246.47790	-23.50844	1.0	5.07	101.53	77.7	1.0	171.8	179.0	76	246.32029	-23.35975	1.6	8.80	75.89	4.2	0.3	26.1	19.3
32	246.48393	-23.50664	1.7	5.38	47.48	0.7	0.2	8.0	1.2	77	246.48702	-23.35644	3.9	9.85	58.51	1.0	0.2	6.4	1.5
33	246.16256	-23.50487	4.7	12.39	71.97	1.6	0.3	8.3	2.7	78	246.22609	-23.35087	3.2	12.30	74.42	5.4	0.4	23.1	5.7
34	246.30824	-23.50337	2.4	4.40	131.63	0.2	0.1	4.8	0.3	79	246.22945	-23.34635	2.7	12.36	75.86	0.8	0.2	8.3	1.5
35	246.42445	-23.49805	3.2	2.06	126.69	0.3	0.1	4.6	0.4	80	246.35589	-23.33620	2.8	9.55	67.53	2.4	0.3	13.9	4.0
36	246.28996	-23.49029	3.4	5.36	126.81	0.7	0.1	8.6	1.0	81	246.36928	-23.33467	1.7	9.54	68.23	12.7	0.6	45.7	24.5
37	246.56058	-23.48891	1.7	9.53	66.97	0.3	0.1	4.8	0.5	82	246.52030	-23.32785	2.9	12.31	53.53	0.9	0.2	6.4	1.3
38	246.43710	-23.48494	1.4	2.78	123.39	15.4	0.5	76.2	52.2	83	246.46964	-23.32679	1.8	10.94	54.82	58.2	1.0	94.3	76.7
39	246.60808	-23.47868	5.9	12.17	49.96	1.3	0.3	4.8	1.9	84	246.29411	-23.32092	1.2	11.52	74.59	46.4	1.0	103.9	60.1
40	246.25135	-23.47380	2.7	7.57	108.56	1.6	0.2	15.2	2.4	85	246.30893	-23.31346	3.1	11.60	59.41	2.0	0.3	10.7	3.0
41	246.41984	-23.46983	1.2	2.26	131.01	24.3	0.6	105.6	33.1	86	246.47738	-23.27933	2.0	13.73	42.00	1.0	0.2	7.5	1.8
42	246.53912	-23.46646	3.9	8.50	72.53	2.7	0.3	14.7	4.1	87	246.51560	-23.26431	1.7	15.42	25.88	0.9	0.3	5.8	1.4
43	246.54110	-23.46385	1.9	8.64	71.22	0.3	0.1	5.2	0.7	88	246.40692	-23.25975	3.1	14.02	42.05	2.8	0.4	11.6	4.4
44	246.14878	-23.46293	1.9	13.25	28.78	28.3	1.0	45.4	42.1	89	246.32039	-23.25723	3.0	14.61	42.62	0.9	0.2	5.5	1.3
45	246.28951	-23.46172	5.6	5.70	127.71	0.6	0.1	5.4	0.9										

Table C.1. WISE and 2MASS photometry of the IR counterparts to X-ray sources. Proper motions from *All WISE* catalog are listed.

Src	Designation	RA (J2000)	Dec (J2000)	[3.4]	e([3.4])	[4.6]	e([4.6])	[12]	e([12])	[22]	e([22])	J	e(J)	H	e(H)	K_s	e(K_s)	pmRA	pmDec	sep	Flag
		deg	deg							mag								mas yr^{-1}		$''$	
1	J162602.17-234051.9	246.5091	-23.6811	9.92	0.02	9.68	0.02	9.18	0.04	6.78	0.10	11.51	0.02	10.57	0.02	10.17	0.02	-25.00	79.00	3.00	III
10	J162543.81-233518.2	246.4325	-23.5884	15.33	0.06	14.94	0.10	12.25	0.53	8.99								296.00	-1352.00	3.40	
12	J162522.43-233501.1	246.3435	-23.5837	9.28	0.02	9.21	0.02	9.25	0.04	8.16		10.70	0.02	9.71	0.02	9.40	0.02	-36.00	-42.00	4.20	III
16	J162606.27-233403.7	246.5261	-23.5677	11.46	0.02	11.17	0.02	10.65	0.27	8.18	0.36	13.14	0.02	12.27	0.03	11.75	0.02	-30.00	47.00	5.40	III
17	J162455.82-233347.9	246.2326	-23.5633	9.14	0.02	9.04	0.02	8.94	0.05	8.68		10.77	0.02	9.77	0.03	9.36	0.02	-144.00	126.00	2.30	III
18	J162542.92-233333.6	246.4289	-23.5593	14.55	0.04	14.54	0.07	11.51	0.33	8.31	0.31	15.91	0.08	15.15	0.08	14.79	0.11	267.00	274.00	5.40	
19	J162515.12-233308.8	246.3130	-23.5525	12.08	0.02	11.90	0.02	8.97	0.06	6.78	0.10	13.73	0.03	12.73	0.02	12.30	0.03	-194.00	106.00	1.60	
20	J162535.03-233255.2	246.3960	-23.5487	8.72	0.02	8.66	0.02	8.57	0.03	8.14	0.27	10.08	0.02	9.21	0.02	8.91	0.02	-98.00	22.00	3.80	III
26	J162537.38-233149.3	246.4058	-23.5304	9.67	0.02	9.53	0.02	9.19	0.04	7.77	0.25	11.09	0.02	10.16	0.02	9.83	0.02	-136.00	-21.00	1.30	III
30	J162523.74-233038.7	246.3489	-23.5108	9.68	0.02	9.56	0.02	9.65	0.08	8.38		11.13	0.03	10.20	0.02	9.87	0.02	44.00	-34.00	0.90	III
31	J162554.61-233029.9	246.4776	-23.5083	8.20	0.02	8.09	0.02	8.01	0.02	7.92	0.23	9.76	0.03	8.81	0.02	8.51	0.02	-23.00	16.00	1.10	III
33	J162438.72-233017.8	246.1614	-23.5050	12.22	0.10	12.21	0.10	11.32	0.36	8.11		14.16	0.04	13.10	0.04	12.74	0.04			3.90	
33	J162438.97-233021.5	246.1624	-23.5060	10.08	0.03	9.89	0.02	9.52	0.07	7.82	0.33	11.71	0.02	10.68	0.02	10.26	0.02	-325.00	40.00	4.10	
38	J162544.78-232905.6	246.4366	-23.4849	9.21	0.02	8.98	0.02	8.99	0.04	8.29		10.78	0.03	9.88	0.04	9.44	0.02	-156.00	-68.00	1.60	III
40	J162500.23-232825.1	246.2510	-23.4737	12.30	0.02	12.01	0.02	11.15		8.83		14.09	0.03	13.08	0.03	12.62	0.03	14.00	-24.00	1.40	
41	J162540.66-232811.3	246.4194	-23.4698	9.06	0.02	9.02	0.02	8.70	0.05	5.31	0.05	10.45	0.02	9.53	0.02	9.25	0.02	-24.00	-13.00	1.40	III
42	J162609.65-232800.9	246.5402	-23.4669	15.90	0.07	15.75	0.17	12.32		8.84								819.00	514.00	4.00	
46	J162546.72-232737.0	246.4447	-23.4603	9.57	0.02	9.45	0.02	9.60	0.06	8.80		11.02	0.02	10.09	0.03	9.77	0.02	-82.00	18.00	0.90	III
47	J162515.02-232713.8	246.3126	-23.4538	10.74	0.02	10.46	0.02	10.31	0.15	7.92		12.15	0.02	11.30	0.02	10.93	0.02	-164.00	26.00	1.60	III
48	J162517.82-232713.1	246.3243	-23.4537	9.07	0.02	8.94	0.02	8.81	0.05	8.19		10.46	0.02	9.54	0.02	9.25	0.02	-114.00	87.00	1.50	III
50	J162535.09-232648.8	246.3962	-23.4469	3.52	0.38	3.19	0.24	3.55	0.02	3.52	0.02	3.57	0.29	3.35	0.25	3.17	0.52	554.00	846.00	1.00	
51	J162531.77-232646.1	246.3824	-23.4462	9.54	0.02	9.29	0.02	9.41	0.07	7.14	0.14							-35.00	105.00	1.10	III
52	J162539.42-232642.2	246.4143	-23.4451	9.13	0.02	8.64	0.02	6.79	0.02	5.04	0.04	10.96	0.02	10.03	0.03	9.57	0.02	-18.00	21.00	5.30	DD
53	J162532.53-232626.7	246.3856	-23.4408	9.23	0.02	8.97	0.02	7.54	0.02	4.48	0.02	10.88	0.04	10.03	0.03	9.69	0.02	-176.00	134.00	0.80	DD
55	J162616.91-232605.5	246.5705	-23.4349	16.14	0.09	15.02	0.10	11.66	0.34	8.39								-513.00	-110.00	1.90	
56	J162620.73-232526.4	246.5864	-23.4240	15.72	0.07	14.90	0.09	10.38	0.11	7.80	0.26							-1701.00	851.00	5.80	
57	J162542.88-232526.4	246.4287	-23.4240	8.59	0.02	8.16	0.02	6.53	0.02	4.43	0.03	10.70	0.03	9.62	0.02	9.20	0.02	-161.00	108.00	0.70	DD
58	J162538.89-232523.7	246.4121	-23.4233	9.95	0.02	9.71	0.02	9.64	0.06	8.74		11.39	0.02	10.56	0.03	10.17	0.02	-30.00	46.00	2.50	III
61	J162555.12-232424.7	246.4797	-23.4069	9.42	0.02	9.27	0.02	9.05	0.04	8.16	0.29	10.99	0.03	9.95	0.02	9.64	0.02	-136.00	25.00	0.90	III
62	J162534.97-232417.5	246.3957	-23.4049	6.29	0.06	6.12	0.04	5.90	0.02	5.66	0.05	6.11	0.02	5.92	0.04	5.78	0.02	-1746.00	1090.00	3.20	
64	J162538.17-232402.3	246.4090	-23.4006	12.85	0.02	12.96	0.03	11.64		8.98		14.61	0.03	13.78	0.02	13.49	0.04	180.00	-342.00	1.60	
66	J162540.29-232352.6	246.4179	-23.3980	12.28	0.02	12.03	0.02	11.37		8.90		13.51	0.03	12.85	0.03	12.50	0.03	-144.00	80.00	2.60	III
67	J162556.39-232346.7	246.4850	-23.3963	15.66	0.07	14.92	0.10	11.17	0.24	8.41								412.00	589.00	2.90	
69	J162545.84-232252.9	246.4410	-23.3814	15.04	0.05	15.03	0.11	11.84		8.30		16.28	0.09	15.37	0.10	14.90	0.13	-228.00	100.00	3.70	
71	J162516.88-232203.4	246.3204	-23.3676	8.80	0.02	8.70	0.02	8.59	0.04	7.13	0.19	10.19	0.02	9.32	0.02	9.02	0.02	-35.00	162.00	2.40	III
72	J162557.23-232158.8	246.4885	-23.3664	12.62	0.02	12.47	0.03	11.06	0.33	8.05	0.36	13.75	0.03	13.11	0.03	12.79	0.03	-217.00	238.00	1.50	
74	J162502.36-232145.0	246.2599	-23.3625	9.14	0.02	9.06	0.02	8.82	0.05	7.99		10.47	0.02	9.58	0.02	9.29	0.02	-25.00	79.00	0.60	III
76	J162516.84-232135.0	246.3202	-23.3597	9.88	0.02	9.73	0.02	9.29	0.05	7.78	0.21	11.32	0.02	10.43	0.02	10.12	0.02	-16.00	248.00	0.30	
78	J162454.14-232104.7	246.2256	-23.3513	15.49	0.07	14.21	0.06	11.35	0.34	8.21	0.40							402.00	-726.00	2.30	
79	J162454.90-232049.2	246.2288	-23.3470	10.65	0.02	10.38	0.02	10.14	0.12	7.77	0.41	12.00	0.02	11.23	0.02	10.87	0.02	-88.00	141.00	3.30	III
80	J162525.36-232009.6	246.3557	-23.3360	16.67	0.15	15.89	0.22	11.39		8.32	0.42							-888.00	2084.00	1.00	
81	J162528.54-232004.9	246.3689	-23.3347	15.20	0.05	14.11	0.06	10.95	0.17	7.87	0.47							-552.00	7.00	1.20	
83	J162552.82-231936.5	246.4701	-23.3268	7.67	0.03	7.56	0.02	7.43	0.02	7.51	0.23	9.26	0.02	8.21	0.04	7.87	0.03	-67.00	173.00	1.50	III
84	J162510.50-231914.7	246.2938	-23.3208	6.95	0.06	6.55	0.02	4.74	0.02	2.25	0.02	9.13	0.02	8.07	0.03	7.51	0.03	54.00	-12.00	1.30	
86	J162554.44-231645.3	246.4769	-23.2793	10.06	0.02	9.84	0.02	9.42	0.05	8.70		11.65	0.03	10.69	0.02	10.30	0.02	-96.00	48.00	1.70	III
87	J162603.70-231553.7	246.5154	-23.2649	15.88	0.08	14.69	0.08	12.10	0.47	8.33								496.00	37.00	2.30	
88	J162537.55-231537.3	246.4065	-23.2604	16.34	0.13	15.34	0.14	11.57	0.40	7.39								390.00	401.00	2.70	
89	J162516.66-231522.4	246.3194	-23.2562	15.69	0.06	14.95	0.10	11.12	0.20	8.59								197.00	-2933.00	4.70	

Table D.1. Best fit parameters from spectral analysis of bright X-ray sources. Notes: for source nr. 41 we give the best fit of the average spectrum, the flare spectrum and post-flare spectrum. For source 62 we give the best fit of the average spectrum, while detailed spectroscopy is given in Table 2.

Src.	Camera	Model	Chi2	DOF	Nh	eNh	kT_1	α	ekT_1	N_1	eN_1	kT_2	ekT_2	N_2	eN_2	kT_3	ekT_3	N_3	eN_3	flux
					cm^{-2}	cm^{-2}	keV		keV	cm^{-5}	cm^{-5}	keV	keV	cm^{-5}	cm^{-5}	keV	keV	cm^{-5}	cm^{-5}	erg s^{-1}cm^{-2}
1	EPIC	1T	56.32	44	0.36	0.03	2.5	1.8	0.21	8.00e-04	7.00e-05	–	–	–	–	–	–	–	–	8.7e-13
12N	EPIC	1T	83.89	44	0.22	0.10	0.95	1.5	0.05	4.60e-05	1.00e-05	–	–	–	–	–	–	–	–	5.7e-14
17	EPIC	2T	105.20	77	0.43	0.04	0.85	1.4	0.05	1.00e-04	2.50e-05	1.8	0.11	2.40e-04	1.50e-05	–	–	–	–	3.9e-13
20	MOS	1T	91.20	59	0.33	0.04	1	0.15	0.04	7.01e-04	6.40e-05	–	–	–	–	–	–	–	–	5e-13
26	EPIC	1T	35.50	29	0.29	0.05	1	0.88	0.05	8.00e-05	1.30e-05	–	–	–	–	–	–	–	–	6.7e-14
30	EPIC	1T	12.70	19	0.31	0.09	0.88	0.23	0.08	6.00e-05	2.00e-05	–	–	–	–	–	–	–	–	5.8e-14
31	EPIC	3T	178.20	133	0.50	0.06	0.23	0.93	0.02	1.60e-03	1.00e-03	1.1	0.04	1.00e-03	2.00e-04	2.1	0.56	2.50e-04	1.40e-04	1.8e-12
38	EPIC	2T	66.70	61	0.55	0.08	0.24	0.93	0.03	8.20e-04	5.20e-04	1	0.07	2.08e-04	3.00e-05	–	–	–	–	5.2e-13
41	EPIC	2T	115.00	90	0.20	0.30	0.99	0.93	0.03	8.10e-04	8.00e-06	2.4	0.21	1.10e-04	1.10e-05	–	–	–	–	2.3e-13
41 Flare	EPIC	2T	49.70	29	0.20	–	0.93	0.93	–	7.20e-05	–	2.5	0.21	3.10e-04	2.00e-05	–	–	–	–	4.6e-13
41 Post-Flare	EPIC	2T	77.04	64	0.20	0.30	0.93	0.93	0.04	7.20e-05	1.00e-05	2.2	0.23	9.40e-05	1.10e-05	–	–	–	–	2e-13
46	EPIC	1T	40.90	28	0.29	0.06	0.93	0.93	0.05	5.00e-05	6.00e-06	–	–	–	–	–	–	–	–	6.1e-13
48	EPIC	2T	62.20	57	0.27	0.06	0.99	0.93	0.05	1.18e-04	3.00e-05	2.5	0.4	–	–	–	–	–	–	3.3e-13
50	EPIC	3T	252.60	207	0.48	0.04	0.24	0.93	0.02	2.28e-03	9.00e-04	1	0.02	1.64e-03	2.00e-04	3.4	0.72	3.90e-04	1.00e-04	3e-12
52	MOS	1T	14.70	10	0.63	0.24	1.1	0.93	0.24	8.00e-05	3.00e-05	–	–	–	–	–	–	–	–	9e-14
58	PN	1T	1.55	4	0.65	0.13	0.6	0.93	0.12	5.00e-05	2.40e-05	–	–	–	–	–	–	–	–	5.9e-14
61	PN	1T	57.10	39	0.42	0.03	2.4	0.93	0.17	1.30e-03	1.20e-04	–	–	–	–	–	–	–	–	1.4e-12
62	EPIC	3T	265.60	225	0.52	0.04	0.3	0.93	0.03	1.80e-03	8.00e-04	1.1	0.02	2.05e-03	2.10e-04	5.4	1.4	4.20e-04	8.00e-05	3.1e-12
71	PN	3T	41.00	39	0.40	0.08	0.24	0.93	0.05	5.30e-04	5.50e-04	1	0.09	3.60e-04	2.00e-04	1.9	0.4	2.10e-04	1.30e-04	6.9e-13
74	EPIC	1T	28.10	22	0.56	0.09	0.93	0.93	0.08	1.20e-04	2.20e-05	–	–	–	–	–	–	–	–	1.5e-13
76	EPIC	1T	22.00	16	0.64	0.07	0.75	0.93	0.06	1.50e-04	3.00e-05	–	–	–	–	–	–	–	–	1.9e-13
79	EPIC	1T	1.40	1	0.06	0.05	1.3	0.93	0.13	1.33e-05	3.00e-06	–	–	–	–	–	–	–	–	1.5e-14
83	EPIC	2T	78.40	69	0.49	0.04	1	0.93	0.04	7.10e-04	2.30e-04	2.9	1.4	1.60e-04	1.00e-04	–	–	–	–	7.7e-13
84	EPIC	2T	108.70	84	0.35	0.02	0.83	0.93	0.04	3.00e-04	7.00e-05	1.6	0.1	3.30e-04	4.00e-05	–	–	–	–	6e-13

Src.	Camera	Model	Chi2	DOF	N_H	eN_H	error	Norm	e.Norm	flux
					cm^{-2}			cm^{-5}		erg s^{-1}cm^{-2}
12S	EPIC	Pow	83.89	44	0.45	0.30	0.23	2.20e-05	7.00e-06	1.3e-13
44	EPIC	Pow	27.20	22	0.52	0.10	0.15	6.00e-05	1.00e-05	4.2e-13
54	MOS	Pow	36.00	25	0.71	0.13	0.15	5.50e-05	1.00e-05	4.5e-13
78	EPIC	Pow	1.73	2	0.33	0.16	0.33	8.00e-06	3.00e-06	5.7e-14
81	EPIC	Pow	27.34	31	0.71	0.10	0.12	4.00e-05	6.00e-06	2.5e-13

Table E.1. Parameters of bestfit to SEDs.

Source	Model	$T_{\rm eff}$ K	$e(T_{\rm eff})$ K	$\log g$ cm s^{-2}	$e(\log g)$ cm s^{-2}	Metallicity	e(Met.)	$F_{\rm tot}$ erg s^{-1}cm^2	$e(F_{\rm tot})$ erg s^{-1}cm^2	$L_{\rm bol}$ $L_{\rm bol,\odot}$	$e(L_{\rm bol})$ $L_{\rm bol,\odot}$	Mass $M_\odot$	Age Myr
1	bt-settl-cifist	3300	61	4.0	0.3	0.0	0.0	2.45e-10	8.1e-12	1.10e-01	3.6e-03	0.26	3.0
12	cond00	4000	38	4.5	0.3	0.0	0.0	5.57e-10	1.4e-11	2.50e-01	6.4e-03	0.88	20.0
16	cond00	3000	93	3.5	0.4	0.0	0.0	5.49e-11	2.3e-12	2.46e-02	1.0e-03	0.10	5.2
20	bt-nextgen-agss2009	5100	119	1.0	0.7	-1.0	0.5	1.87e-09	1.4e-10	8.38e-01	6.4e-02	—	—
26	bt-nextgen-gns93	3600	71	4.0	0.4	0.0	0.2	3.23e-10	1.7e-11	1.45e-01	7.5e-03	—	—
30	dusty00	3700	88	4.5	0.2	—	—	3.45e-10	1.7e-11	1.55e-01	7.7e-03	0.68	14.4
31	bt-settl	4800	112	-0.5	0.2	-1.5	0.7	2.60e-09	1.9e-10	1.17e+00	8.6e-02	1.20	—
38	cond00	3500	58	4.5	0.2	0.0	0.0	5.06e-10	1.9e-11	2.27e-01	8.6e-03	0.46	3.5
41	bt-nextgen-agss2009	4300	89	-0.5	0.1	-1.0	0.6	7.88e-10	4.6e-11	3.54e-01	2.0e-02	—	—
46	Kurucz	3750	76	5.0	0.2	0.5	0.2	4.18e-10	1.9e-11	1.88e-01	8.5e-03	0.50	7.1
47	dusty00	3300	68	4.0	0.4	—	—	1.14e-10	5.3e-12	5.14e-02	2.4e-03	0.25	8.7
48	bt-settl-cifist	3700	86	4.5	0.3	0.0	0.0	5.92e-10	3.3e-11	2.66e-01	1.5e-02	0.50	3.0
52	cond00	3100	113	4.5	0.6	0.0	0.0	4.71e-10	2.4e-11	2.11e-01	1.1e-02	—	—
57	bt-settl-cifist	4200	105	5.5	0.3	0.0	0.0	9.72e-10	6.0e-11	4.36e-01	2.7e-02	0.90	7.5
58	dusty00	3300	46	4.0	0.2	—	—	2.38e-10	8.7e-12	1.07e-01	3.9e-03	0.28	3.7
61	bt-nextgen-agss2009	3600	67	4.0	0.4	0.0	0.3	3.98e-10	1.6e-11	1.79e-01	7.1e-03	—	—
66	Kurucz	3500	0	5.0	0.0	0.0	0.2	3.59e-11	9.1e-13	1.61e-02	4.1e-04	0.30	90.4
71	bt-settl-cifist	3900	102	5.5	0.3	0.0	0.0	8.38e-10	5.0e-11	3.76e-01	2.2e-02	0.62	3.4
74	bt-nextgen-gns93	4000	112	5.0	0.3	0.3	0.1	6.27e-10	4.3e-11	2.82e-01	1.9e-02	—	—
79	dusty00	3300	91	5.0	0.6	—	—	1.25e-10	6.5e-12	5.61e-02	2.9e-03	0.25	7.9
86	cond00	3100	50	4.5	0.2	0.0	0.0	1.66e-10	3.0e-12	7.44e-02	1.4e-02	0.16	2.1

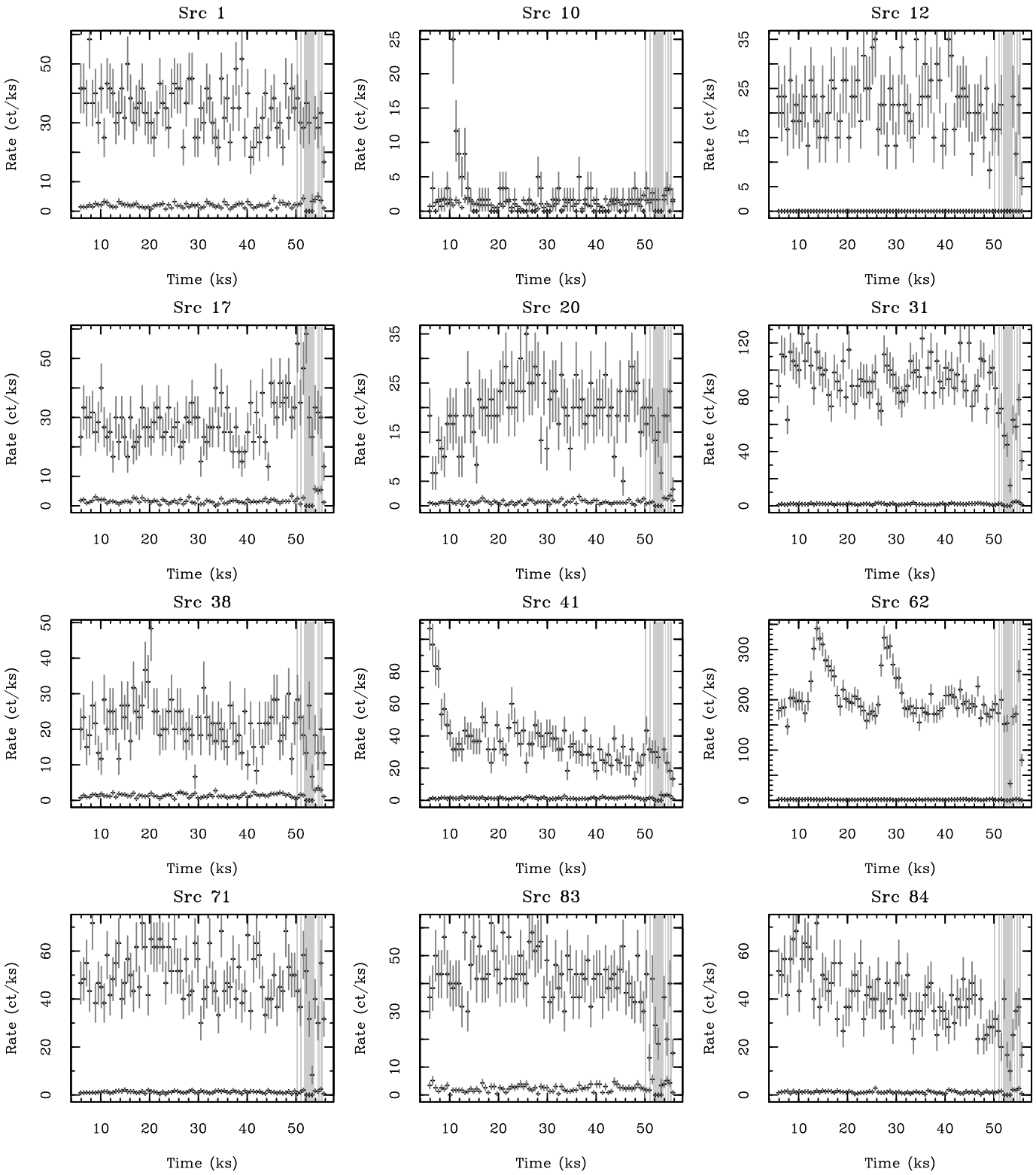

Fig. F.1. PN light curves of brightest X-ray sources and showing variability at $> 1\sigma$ level. Light curves of scaled background are also shown. Sources 10, 38, 41 and 62 show clear flare-like variability. Gray areas represent the high background intervals filtered out for optimizing the source detection effectiveness toward faint sources. Source 62 (ρ Ophiuchi C) is discussed in details in Sect. 3.5.2. The light curve of source 50 (ρ Ophiuchi A+B) is not shown here, its analysis is detailed in Pillitteri et al. (2014).